

UNITED STATES AIR FORCE
SCHOOL OF AEROSPACE MEDICINE

LASER SINTERED CALCIUM
PHOSPHATE BONE

Neal K. Vail
W. Casey Fox

BIOMEDICAL ENTERPRISES, INC
14785 OMICRON DRIVE, SUITE 205
SAN ANTONIO TX 78245-3223

January 1999

19990202 063

USAF DENTAL INVESTIGATION SERVICES
2509 KENNEDY CIRCLE
BROOKS AFB TX 78235-5117

Approved for public release; distribution unlimited.

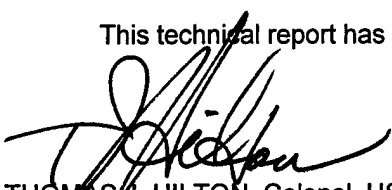
NOTICES

This report is published in the interest of scientific and technical information exchange and does not constitute approval or disapproval of its ideas or findings.

Using Government drawings, specifications, or other data included in this document for any purpose other than Government procurement does not in any way obligate the US Government. The fact that the Government formulated or supplied the drawings, specifications, or other data does not license the holder or any other person or corporation; or convey any rights or permission to manufacture, use, or sell any patented invention that may relate to them.

The Office of Public Affairs has reviewed this technical report, and it is releasable to the National Technical Information Service, where it will be available to the general public, including foreign nationals.

This technical report has been reviewed and is approved for publication.



THOMAS J. HILTON, Colonel, USAF, DC
Chief, Dental Investigation Service

REPORT DOCUMENTATION PAGE			Form Approved OMB No. 0704-0188
<p>Public reporting burden for this collection of information is estimated to average 1 hour per response, including the time for reviewing instructions, searching existing data sources, gathering and maintaining the data needed, and completing and reviewing the collection of information. Send comments regarding this burden estimate or any other aspect of this collection of information, including suggestions for reducing this burden, to Washington Headquarters Services, Directorate for Information Operations and Reports, 1215 Jefferson Davis Highway, Suite 1204, Arlington, VA 22202-4302, and to the Office of Management and Budget, Paperwork Reduction Project (0704-0188), Washington, DC 20503.</p>			
1. AGENCY USE ONLY (Leave blank)	2. REPORT DATE	3. REPORT TYPE AND DATES COVERED	
	January 1999	Final - 2 Jan 97 - 9 Dec 98	
4. TITLE AND SUBTITLE Laser Sintered Calcium Phosphate Bone			5. FUNDING NUMBERS C - F41624-97-C-2000 PE - 65502F PR - STTR TA - AD WU - 61
6. AUTHOR(S) Neil K. Vail W. Casey Fox			
7. PERFORMING ORGANIZATION NAME(S) AND ADDRESS(ES) BioMedical Enterprises, Inc 14785 Omicron Drive, Suite 205 San Antonio, TX 78245-3223			8. PERFORMING ORGANIZATION REPORT NUMBER
9. SPONSORING/MONITORING AGENCY NAME(S) AND ADDRESS(ES) School of Aerospace Medicine USAF Dental Investigation Service 2509 Kennedy Circle Brooks AFB TX 78235-5117			10. SPONSORING/MONITORING AGENCY REPORT NUMBER SAM-AF-BR-TR-1998-0002
11. SUPPLEMENTARY NOTES School of Aerospace Medicine Technical Monitor: Col Thomas J. Hilton, USAFSAM/AFD, (210) 536-3502			
12a. DISTRIBUTION AVAILABILITY STATEMENT Approved for public release; distribution unlimited.		12b. DISTRIBUTION CODE	
13. ABSTRACT (Maximum 200 words) BioMedical Enterprises, Inc collaborated with The University of Texas at Austin (UT-Austin) and The University of Texas Health Science Center at San Antonio (UTHSCSA) to develop methods and systems for the fabrication of complex three-dimensional porous bone structures from calcium phosphate ceramics using the rapid prototyping (RP) technology selective laser sintering (SLS). BME has successfully implemented a pilot facility to fabricate calcium phosphate implants using anatomical data coupled with the selective laser sintering process. Fabrication of commodity and anatomical shapes has been demonstrated. Work is continuing to streamline the pilot facility to efficiently and reproducibly fabricate calcium phosphate implants with desired mechanical, physical, and dimensional properties.			
14. SUBJECT TERMS Biocompatible, Bone, Calcium phosphate, Ceramic, Custom implant, Laser sintering			15. NUMBER OF PAGES 39
16. PRICE CODE			
17. SECURITY CLASSIFICATION OF REPORT Unclassified	18. SECURITY CLASSIFICATION OF THIS PAGE Unclassified	19. SECURITY CLASSIFICATION OF ABSTRACT Unclassified	20. LIMITATION OF ABSTRACT UL

Table of Contents

List of Tables	i
List of Figures	i
Introduction.....	1
Background.....	1
Objective	2
Results by Task Group	2
Task Group 1 - Implant Manufacturing	2
Task Group 2 - Implant Design	4
Task Group 3 - Materials Formulation	8
Task Group 4 - Preclinical Evaluation.....	29
Task Group 5 - Medical Standardization	31
Task Group 6 - FDA Milestones	32
Conclusions.....	33
References.....	33

List of Tables

Table 1. Polymer synthesis	1
Table 2. Comparison of advantages and disadvantages of encapsulation processes	13
Table 3. Summary of microencapsulation experiments	14
Table 4. Fluidized bed microencapsulation process operating conditions	14
Table 5. Raw materials list and suppliers	32

List of Figures

Figure 1. Laser sintering process	1
Figure 2. Implant design process flow chart	4
Figure 3. Computed tomography image of an <i>ex vivo</i> baboon skull	5
Figure 4. Computed tomography image of human patient	5
Figure 5. Velocity interface	6
Figure 6. 3-D reconstruction of a human condyle	6
Figure 7. 3-D reconstruction of a human zygomatic arch	6
Figure 8. 3-D reconstruction of mandibular angle with fixation features	7
Figure 9. 3-D reconstruction of mandibular angle with macropore structures	7
Figure 10. Fabrication of custom implants via selective laser sintering	9
Figure 11. SEM of +106-125 μ m calcium phosphate powder	10
Figure 12. Polymer binder melt flow viscosity	12
Figure 13. Polymer binder bulk mechanical properties	12
Figure 14. SEM of +45-63 μ m spheroidized soda-lime glass	15
Figure 15. SEM of polymer encapsulated +45-63 μ m spheroidized soda-lime glass	15
Figure 16. Particle size distributions of coated and uncoated glass substrates	15
Figure 17. PSD dimensional changes	15
Figure 18. Particle size distribution of calcium phosphate powders	16
Figure 19. SEM of encapsulated calcium phosphate powder	16
Figure 20. Fabrication orientation of strength specimens	18
Figure 21. Three-point bend strength of SLS fabricated specimens	19
Figure 22. Compressive strength of SLS fabricated specimens	19

Figure 23. Material shrinkage calibration for +106-125 μ m calcium phosphate	20
Figure 24. Material shrinkage calibration verification	20
Figure 25. Post-processing process schematic	21
Figure 26. Drying extents	23
Figure 27. Firing cycle profile	24
Figure 28. Compression test specimen geometry	24
Figure 29. Solid uptake with infiltrating solution composition	25
Figure 30. Compressive strengths and moduli after 1 hour at 800°C	26
Figure 31. Linear shrinkage after 1 hour at 800°C	26
Figure 32. Compressive strengths at all firing conditions	26
Figure 33. Linear shrinkages at all firing conditions	26
Figure 34. Compressive strengths and moduli as function of relative part density	26
Figure 35. Pore size distribution of post-processed calcium phosphate specimen	27
Figure 36. Unit cell configuration	27
Figure 37. Common implant shapes fabricated by selective laser sintering	29
Figure 38. Superior view of supra orbital fabricated by selective laser sintering	29
Figure 39. Canine alveolar ridge implant geometry	29
Figure 40. Radiograph of SLS fabricated canine implant <i>in vivo</i>	30
Figure 41. Histology image of SLS fabricated canine implant	30
Figure 42. Proposed time line for alveolar ridge defect study in pigs	31

Introduction

BioMedical Enterprises, Inc collaborated with The University of Texas at Austin (UT-Austin) and The University of Texas Health Science Center at San Antonio (UTHSCSA) to develop methods and systems for the fabrication of complex three-dimensional porous bone structures from calcium phosphate ceramics using the rapid prototyping (RP) technology selective laser sintering (SLS).

Background

Impetus for the present work stems from a body of related work dating to the mid-1980's. In 1987, Capano and Lagow at UT-Austin published results pertaining to the synthesis of porous calcium phosphates of diverse compositional makeup for use as bone implant materials.¹ They subsequently reported biocompatibility results for implants comprised of a particular calcium phosphate composition in a canine alveolar ridge defect model.^{2,3} Lagow and coworkers continued their calcium phosphate work to improve mechanical properties, to control material porosity, and to define implant fabrication methods.

During the same time period, Deckard, *et al.*,^{4,5} at UT-Austin, developed the selective laser sintering (SLS) process (figure 1). SLS became part of a group of emerging technologies known collectively as rapid prototyping (RP).⁶ RP presented a new manufacturing approach based on the selective layerwise addition of materials to fabricate objects of complex geometry without part specific tooling. SLS implemented this methodology as the selective layerwise sintering of heat fusible materials with the aid of a high energy scanning laser beam. Theoretically, SLS could be used to fabricate objects from a wide variety of base materials, including metals and ceramics.

Several groups at UT-Austin explored numerous material systems, focusing on direct fabrication of components from structural materials, such as metals and ceramics. However, this quickly proved a long-term endeavor and focus shifted to alternative methods of using SLS to fabricate structural components. Bourell, *et al.*,⁷ proposed the use of multicomponent systems comprised of low and high temperature melting materials. During SLS processing, the low temperature melting material would serve to bond the high temperature material to produce an object comprised of a matrix composite. In one embodiment, the low temperature melting material would be a polymer that could be removed during subsequent post-processing steps leaving the high temperature melting component. This methodology was termed indirect fabrication and was demonstrated by Vail, *et al.*,⁸ for the fabrication of ceramic components.

Parallel to SLS process and material development, other groups were focusing on utilizing SLS, and other RP processes, to fabricate objects from data other than traditional

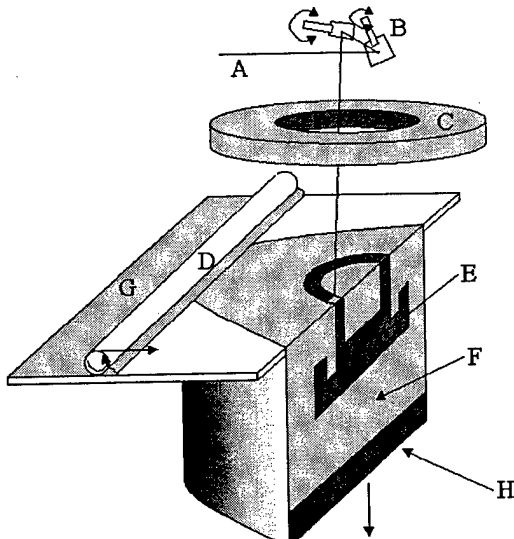


Figure 1. Laser sintering process schematic. A-laser beam; B-scanner mirrors; C-radiant heater; D-powder delivery; E-sintered part; F-unsintered powder bed; G-new powder layer.

two- and three-dimensional computer aided design (CAD) sources. In 1992, Crawford, *et al.*, demonstrated the real time fabrication of a reverse engineered object. In this example, an automobile piston was digitized using industrial computed tomography (CT). The digitized data, available as discrete slice descriptions, were transmitted via conventional telephone communications to the UT-Austin SLS lab where the data were used to fabricate a replica in a thermoplastic material.

Also in 1992, Bartels, *et al.*,⁹ demonstrated the use of SLS to fabricate models of pollen grains in durable ceramic materials using three-dimensional scanning electron microscopy data. In 1993, Levy, *et al.*,¹⁰ fabricated human temporal bone models via SLS using data obtained by medical CT imaging. Concurrently, Lagow and coworkers approached the UT-Austin SLS group to explore the use of SLS to fabricate implants from their calcium phosphate materials.

Lee and Barlow demonstrated the concept of implant fabrication from the Lagow materials using the indirect SLS fabrication methodology developed earlier by Vail, *et al.* The work of Barlow, *et al.*,¹¹ led to a recently issued patent, currently under exclusive license to BioMedical Enterprises, Inc. (BME). To further development work toward eventual commercialization, BME, in cooperation with Barlow, *et al.*, in 1995, obtained a phase I Small Business Technology Transfer (STTR) grant funded through Armstrong Laboratories of the Department of Defense. BME brought significant expertise in the healing of bone as well as in the study of bone treatment modalities in preclinical situations to the custom formed synthetic bone project. Highly encouraging results of the phase I effort, including further materials formulation and two preclinical studies to assess safety and efficacy, led to funding of this phase II STTR effort.

Objective

The objective of the phase II effort was to develop a pilot scale custom formed synthetic bone manufacturing system. Activities of this effort would build on knowledge gained during the phase I effort to establish a reliable system consistent with good manufacturing practices (GMP) precursory to full-scale system implementation. Specific aspects of the objective included 1) medical image data acquisition, implant modeling, and integration of custom features into the implant model; 2) materials formulation both to optimize implant fabrication and to achieve desired implant properties; 3) implant manufacturing; 4) preclinical assessment of SLS fabricated implants; 5) system validation, packaging development, and device tracking methods; and 6) achievement of FDA milestones necessary for commercialization.

Results by Task Group

The proposal for this effort detailed the scope of work as a series of individual tasks. Related tasks were grouped according to the specific aspects of the project objective as described above. This section discusses the results of the respective task groups.

Task Group 1 - Implant Manufacturing

Tasks in this group focused on the implementation of the respective processing facilities to accomplish fabrication of custom formed synthetic bone implants. To this end, BME implemented a data processing laboratory, a materials formulation

laboratory, a powder processing laboratory, and a implant manufacturing and processing laboratory.

The **data processing laboratory** provides the necessary tools to handle processing of medical imaging data, creation of implant models, and integration of custom design features into modeled implants. The laboratory consists of a Silicon Graphics O2 workstation with an Irix/Unix operating system. On this system are installed the medical image processing software package Velocity (Image³, LLC, Salt Lake City, Utah), SDRC-Ideas Master Series 6 CAD/CAM package (Structural Dynamics Research Corporation, Milford, Ohio), and MedLink (Dynamics Computer Resources, San Dimas, Calif.), an data interface tool between Velocity and Ideas. Together, this solution set provides a satisfactory initial solution to the implant design problem (see **Implant Design** discussion). Additionally, the laboratory provides internet access via dial up services. Intranet services are available.

A **materials formulation laboratory** provides the necessary equipment to produce materials used to fabricate custom formed synthetic bone. Particular components of this laboratory are raw materials storage, chemical synthesis equipment, analytical equipment, a convection oven, and a high temperature furnace for powder materials formulation and characterization. Chemical inventories are maintained and corresponding Material Safety Data Sheets (MSDS) are available. Fume hoods and safety equipment are available.

A **powder processing laboratory** provides the necessary equipment to produce and characterize the powder materials used to fabricate custom formed synthetic bone. The laboratory supports powder storage, bulk material comminution, and powder characterization equipment. Comminution equipment consists of a manual roughing mill and motorized refinement mill. Powder produced by these mills are characterized for powder size by a benchtop shaker with sieving screens of various sizes. This combination of equipment provides a satisfactory solution to the powder handling requirements (see **Materials Formulation** below). No microencapsulation facilities were installed during this project.

The **implant fabrication laboratory** contains a SinterStation 2000 (DTM Corporation, Austin, Texas), which implements the selective laser sintering process for commercial applications. Model data are transferred to this workstation by intranet services. The workstation provides remote access capabilities to start, monitor, and terminate the fabrication of implants. The laboratory is equipped with powder storage facilities, workstation facility hookups, environmental monitoring sensors, and safety equipment.

Implant packaging, implant sterilization, and device tracking systems were not implemented during this project but are under investigation.

Summary of Implant Manufacturing

All essential equipment is in place to effectively manufacture custom formed synthetic bone implants on small scale. Some components of the manufacturing facilities would necessarily require further scaling to increase the capacity of the manufacturing process. Additional materials processing and analytical components require specification to facilitate materials formulation (see **Materials Formulation** below) and to provide streamlined process validation precursory to FDA approval.

Task Group 2 - Implant Design

Tasks in this group are related to acquisition of anatomical image data, image data processing and implant modeling, and engineering manipulation of derived implant models to incorporate custom design features including macrotrabeculae, surface textures, and implant fixation mechanisms. The complete design process is illustrated in figure 2. Results of specific components of this task group are discussed below.

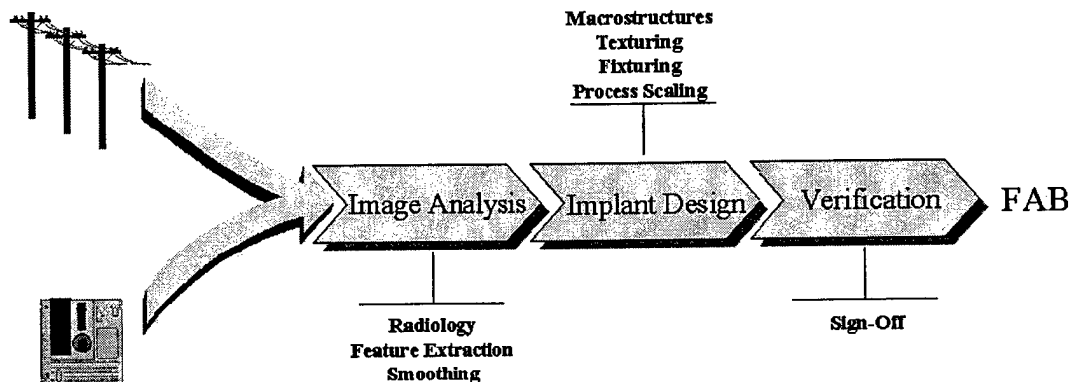


Figure 2. Implant design process flow chart.

Image data were obtained from local institutions. The MacKown Dental Laboratory at Lackland Air Force Base, San Antonio, Texas, provided several anonymous patient data sets from their clinical library. These data were obtained using a General Electric 9800 Computed Tomographic (CT) Scanner. Data were made available on optical disk. BME obtained image data sets of baboon spine segments using a GE HiLite Advantage CT Scanner. These data were made available on 4mm digital audio tape (DAT). BME obtained image data sets of baboon femoral, tibia, and spinal regions using a GE Technicare 1440 CT Scanner. These data were made available on reel-to-reel magnetic tape. BME obtained an image data set of an *ex vivo* baboon skull using a Siemens Somatom Plus. These data were made available on optical disk.

All data required downloading from the provided storage media to BME's image processing platform. Data on 4mm DAT were easily downloaded via a peripheral tape drive. The remaining data sets were transferred to 4mm DAT by a third party vendor who had appropriate hardware. This outsourced media transfer operation typically required about one week to complete.

CT images required extraction from the downloaded data sets. All scanner manufacturers implement different image data set storage formats as well as

different image formats. For example, Siemens stores image data sets as a directory structure followed by an arbitrary list of the images. Simple C/C++ language programs were written to parse the appropriate data sets to extract images. These programs provide rudimentary access to the image directory and allow extraction of individual images or complete patient image sets.

Once images were available, they were easily imported into the image processing software. Figure 3 shows a typical CT image of the *ex vivo* baboon skull obtained at slice resolution of 1mm. These data are very clean and easily processed to produce a three-dimensional model. Figure 4 shows another typical CT image for a human patient. Here the data are less optimal due to the surrounding tissue and to the patient having dental caps, which serve to introduce significant scatter to the surrounding hard tissue data. Scattering can occur in areas of increased hard tissue and scanner operators may adjust exposure radiation intensity during data acquisition to account for changes in tissue density. Manual changes to data acquisition as well as normal changes in tissue density contribute to variations in pixel intensities between images of an image set. BME developed image processing software protocols to homogenize pixel intensities across the image data set to increase hard tissue threshold uniformity and to minimize manual image processing interaction.

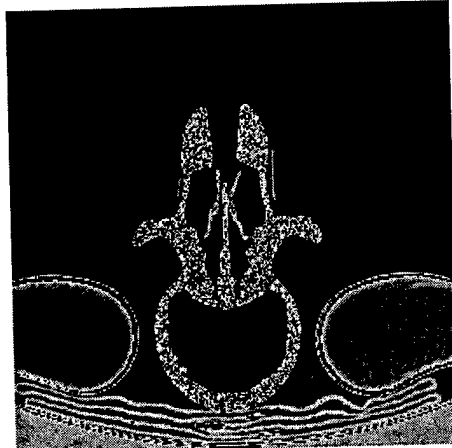


Figure 3. Computed tomography image of an *ex vivo* baboon skull.

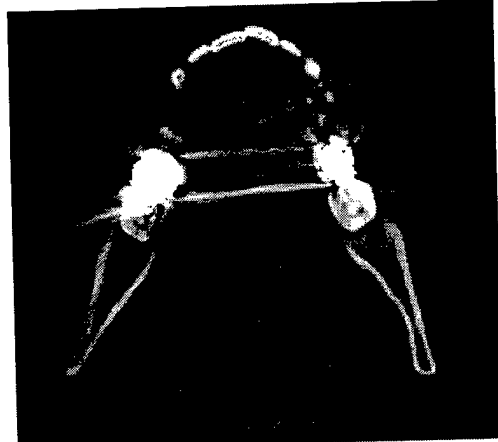


Figure 4. Computed tomography image of a human patient. Patient has dental caps that interfere with the hard tissue data.

Software solutions were put into place to handle CT image data processing. The software suite consists of an image processing package, a CAD/CAM package, and a data translation interface between the image processing package and the CAD/CAM package.

The Velocity image processing software is an elegant package designed specifically for the purpose of working with CT type data (figure 5). The package supports image format converters for common scanners, such as those manufactured by Siemens and GE. The software package provides many useful image processing functions, radiological functions common in CT analysis, and scripting capabilities for task automation. The package provides three-dimensional (3-D) reconstruction capabilities and produces 3-D model files,

which are directly compatible with rapid prototyping systems. However, the software does not provide convenient access to the image libraries produced by commercial CT scanners.

The SDRC-Ideas CAD software is a popular full featured three-dimensional solid modeling and design package. The package allows for design of common and free-form geometry shapes, which have utility in the integration of custom features into implants. However, Ideas does not directly support input of the implant model information produced by the Velocity image processing software. The MedLink software serves as an interface to import anatomical model data into the CAD environment for subsequent sophisticated geometrical manipulation. This interface translates contour information derived from each of the CT slices into b-spline elements supported by SDRC-Ideas. Once all contours are imported, a surface is fitted to the b-splines to produce a solid model. However, this solution is sufficient only for simple anatomical features, in particular, surfaces on the convex hull. For example, one can easily import information about the exterior of a long bone shaft, but not the complete long bone with medullary cavity and distal and proximal features. In this case, the long bone must be decomposed into the individual components of the long bone shaft, the medullary cavity, and the distal and proximal features. In the later cases, these features may require further decomposition due to continued bifurcation conditions. These feature decompositions are performed in the Velocity environment, and imported separately into Ideas. In Ideas, the separate objects are joined together to produce a contiguous model, provided there is exact feature matching (figure 6). Such model specific manipulation is problematic or impossible in more complex feature locations, such as in the craniofacial area (figure 7).

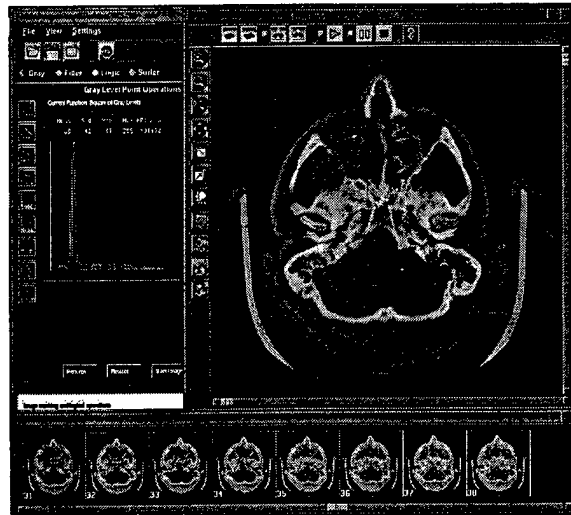


Figure 5. Velocity software.

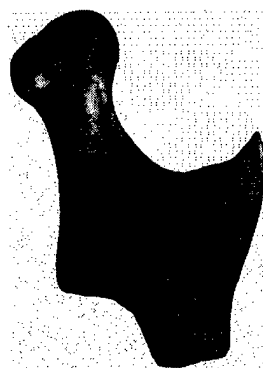


Figure 6. 3-D reconstruction of a human condyle in SDRC-Ideas. Shaded regions show individual components of the model.

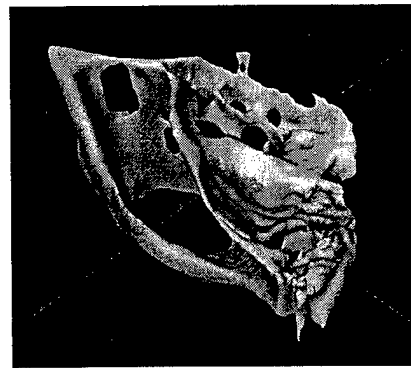


Figure 7. 3-D reconstruction of a human zygomatic arch in Velocity. Note geometric complexity compared to figure 6.

Implant fixation methods were studied using the SDRC-Ideas CAD/CAM software. In one study, a 3-D model of the left mandibular angle of a baboon was manipulated to study various methods of fixturing. Figure 8 shows features added to the angle to accommodate either Steinmann pins or Kirschner wires. In other cases, methods of using bone plates were examined.

Implementation of macrotabecular structures was studied using the SDRC-Ideas CAD/CAM software. Several methods exist for incorporating trabecular structures into 3-D objects. However, simple geometrics, such as bars and rods, can be used to incorporate complex trabecular structures into implants. Figure 9 shows macropore structures added to the same mandibular angle model discussed previously.

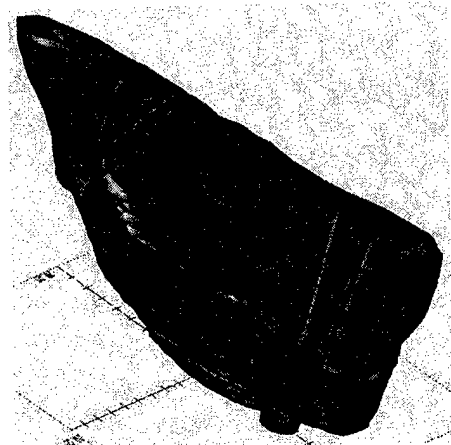


Figure 8. 3-D reconstruction of the mandibular angle of a baboon shown with cutaway to reveal hollow interior with added geometrical features for fixation by pins or wires.

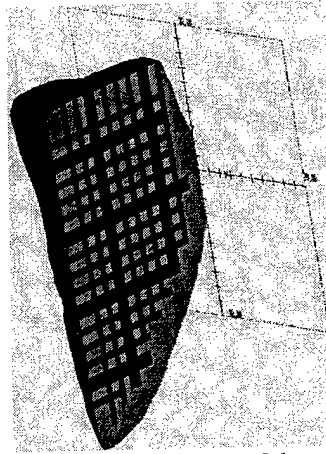


Figure 9. 3-D reconstruction of the mandibular angle of a baboon shown in crosssection to reveal added geometrical features to implement macropore structures.

Summary of Implant Design Tasks

The implemented software suite provides a good solution to limited implant design. The software suite could be improved by the incorporation of additional components to provide an optimal implant design solution. There are two aspects requiring further attention: 1) the interface to stored image data sets and 2) the interface of reconstructed three-dimensional CT model data to the CAD/CAM environment.

In the first case, utility software was created to extract selected images from the image data sets obtained during this effort. This software requires further development to provide seamless access to the original storage media through appropriate hardware considerations. Ideally, this software should be integrated into the image processing package to further optimize the handling of image data sets. BME has entered into agreements with the Velocity software developer to explore this possibility. Parallel to this effort, it is necessary to develop mechanisms to handle image data sets on the native storage media. This

requires a prioritization of the most common storage media types and commitment to the purchase of the associated hardware. A more rigorous approach would be to move CT manufacturers towards support of a common storage format and media type.

Parallel to hardware and data format support issues, consideration needs to be given to high speed transmission of image data that will be required to achieve efficient response to future custom implant fabrication requests. Given the enormous quantity of data in a single image set (typically greater than 25Mb), access to dedicated high speed internet services (*i.e.* ISDN or T1) will be necessary to achieve effective data transferal. In addition, high speed communication capabilities will facilitate virtual conferencing with attending physicians to aid implant design and acceptance.

In the second case, the MedLink interface between the image processing program and the CAD package is severely limited in the present application for several reasons: 1) the reconstruction algorithm is constrained to surfaces on the convex hull; 2) the quantity of data to describe a model is constrained; 3) model reconstruction requires considerable user interaction; and 4) the reconstruction process is $O(n^2)$ in execution time, where n is the number of points describing the model. A more optimal solution to the CAD manipulation of anatomical data would be to perform CAD operations directly on the reconstructed model produced by the image processing software. These models are conveniently exported in the STL format supported by most RP systems. New STL modeling packages have been introduced recently that provide CAD based operations directly on the STL model. These packages provide common CAD functions such as union, intersection, and joining with other STL models or common geometrical shapes.

Further consideration needs to be given both to the method of data acquisition and to the quality of acquired data. Protocols need to be developed to instruct scanner operators on optimal methods of data acquisition, including patient orientation and data acquisition parameters. For example, different patient orientations will be required to capture information about the maxilla area than the mandible area. In the scope of this study no work was done to address the accuracy of the image data with respect to the original object. Such information could be obtained by correlation of defined anatomical features to reconstructed model dimensions. This would necessarily be different for each case. Alternatively, standard dimensional objects, independent of the patient, could be scanned with the patient to provide scaling parameters during image processing. Any such provision for imaging accuracy should be implemented as part of the data acquisition protocol.

Task Group 3 - Materials Formulation

Materials formulation tasks comprised the major component of the phase II effort. Tasks in this group are related to formulation of raw materials, preparation and characterization of powder feedstocks, quantification of SLS process parameters, definition and characterization of post-processing conditions, and characterization and quantification of all material properties. For clarity, the following discussion

presents the materials formulation components in more detailed form than in the project proposal.

Overview of Implant Fabrication Process

Figure 10 shows the generalized method of fabricating calcium phosphate ceramic implants. The major steps of this process include: 1) formulation and characterization of a composite material comprised of a thermoplastic binder and substrate material, 2) selective laser sintering of this dry, free-flowing composite powder to produce a three-dimensional shape (termed a *green part*), and 3) post-processing of the green part to produce a durable ceramic component. The latter step normally consists of a heat treatment to first decompose the thermoplastic binder and then sinter the substrate particles to impart mechanical strength to the fabricated shape. This indirect method of component fabrication is readily practiced using commercial SLS platforms.

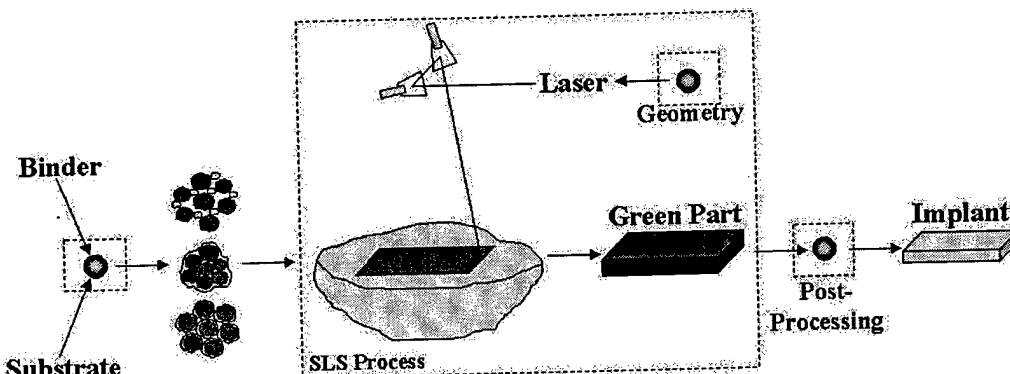
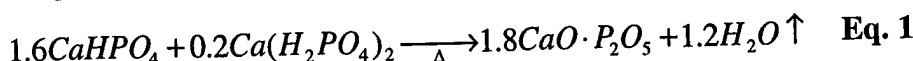


Figure 10. Schematic of the fabrication of custom implants via selective laser sintering. Process is also referred to as indirect fabrication.

Powder formulation, including composition and particle size distribution, was based on results of the phase I effort. Powder properties are constrained by requirements on the final implant. Specifically, the implant is required to be porous with a mean pore size distribution of about $100\mu\text{m}$ and further is required to comprise a calcium phosphate of composition $1.0 > \text{Ca/P} > 0.5$, where Ca/P is the ratio of atomic calcium to atomic phosphorous.

Considering first the powder chemical composition, from known calcium phosphate chemistry, the compositional constraints correspond to the species dicalcium phosphate (DCP, $\text{Ca/P}=1.0$, CaHPO_4) and monocalcium phosphate (MCP, $\text{Ca/P}=0.5$, $\text{Ca}(\text{H}_2\text{PO}_4)_2$), respectively. Both of these calcium phosphates irreversibly convert to different chemical species on heating. DCP polymerizes by successive addition of $-\text{PO}_3$ units and elimination of water to form calcium metaphosphate (CMP, $(\text{CaPO}_3)_n$), a highly crystalline phase of considerable strength, which is a function of the degree of polymerization. MCP eliminates water to form calcium pyrophosphate (CPP, $\text{Ca}_2\text{P}_2\text{O}_7$), another crystalline phase.

The starting substrate powder is a calcium phosphate with $\text{Ca/P}=0.9$, derived through the following reaction of DCP and MCP:



The product is produced in bulk by heating a mixture of the reactants in air to 1000°C for twelve hours to form dense blocks of raw starting material. Material balances confirm the extent of the reaction through loss of water. The existence of the resulting MCP and CPP phase can be confirmed by x-ray diffraction analysis (XRD).

Raw material blocks are comminuted through a two-step process. The blocks are first broken into marble size chunks in a roughing process, then reduced further to less than 150 μ m with a continuous mechanical grinder. In practice, the raw material blocks are extremely hard and difficult to comminute; thus, the heat treatment cycle was modified to aid powder production. A rapid quench from about 500°C or higher produces an amorphous brittle material easily broken by hand.

A powder comprising the particle size fraction +106-125 μ m was the material used in further formulation purposes (figure 11). Choice of this fraction is related primarily to the role of particle size on resulting implant pore size. The necessary powder quantity to perform subsequent material formulation tasks was estimated at about 20kg. The majority of this material would be required for later SLS studies due to the capacity of the commercial platform.

Yield of the specified particle size fraction is less than 20%, which is related to the narrow size range specification. It is interesting to note that comminution tends to produce a bimodal distribution with peaks occurring at about 125 μ m and about 45 μ m with gradual tapering to submicron particle sizes. This is generally indicative of an inefficient grinding process. Sub-45 μ m powder tailings can be reconstituted and comminuted provided no contamination occurs during powder production.

Powder production quantity is limited by the available sieving equipment, which is a benchtop batch system designed primarily for characterization of experimental quantities. Equipment analysis indicates the implementation of a continuous industrial sifter would increase powder throughput by more than tenfold. However, while the present comminution method could supply the increased sifting throughput level, the equipment is not suitable, in the long-term, for the present material system. The material abrasiveness causes spalling of the grinding plates, which introduces metal contamination. This has been confirmed by visual inspection and by chemical analysis. Significant portions of the metal contamination can be removed by washing the powder and magnetic retrieval.

Alternative powder formulation methods were sought to increase powder uniformity and yield and to minimize contamination. Major limitations to finding commercial vendors for the powder are the particle size requirements and the low

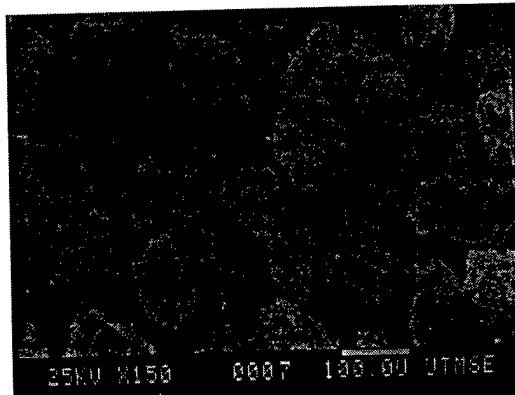


Figure 11. Scanning electron micrograph of characterized calcium phosphate powder (Ca/P=0.9) with particle size distribution of +106-125 μ m.

material volume requirements. VIOX Corporation (Seattle, Wash.), a producer of specialty glasses for the electronics industry, was contacted to study the feasibility of calcium phosphate powder production. VIOX formulates materials in melt and then quenches to form a glass frit, which can be further comminuted by jet milling. This approach offers several advantages to the current powder production method: 1) material homogeneity; 2) reduced contamination; 3) particle size optimization; and 4) volume production.

Preliminary results from VIOX are promising. Homogeneous melts of selected calcium phosphates with $0.5 < \text{Ca/P} < 1.0$ were produced and provided as broken frits. A large batch of raw starting material ($\text{Ca/P}=0.9$) was processed and characterized to +45-125 μm with emphasis on maximizing powder yield to the high end of the distribution. Yield of the specified fraction was about 45% and the powder had a normal distribution with a median particle size of 79 μm . Tailings of this initial formulation will be reconstituted to assess feasibility. Further analysis of the delivered material will include compositional, particle size characterization to +90-125 μm , and scanning electron microscopy (SEM) to assess particle morphology.

Polymer binder was formulated following the methods developed by Vail, *et al.*¹² In that work, the polymer was an 80/20 mol/mol (0.74/0.26 wt./wt.) copolymer of methylmethacrylate (MMA) and *n*-butylmethacrylate (*n*BMA) with a typical glass transition temperature, T_g , of about 85-90°C. The methacrylate based copolymer was chosen to ensure complete thermal decomposition to gaseous by-products during post-processing. The copolymer was formulated to have a specific melt viscosity through molecular weight control during polymerization. Controlled melt viscosity optimized binder performance during SLS processing while concurrently maintaining a high bulk mechanical strength to achieve strong green parts.

In the present effort, the copolymer constituent composition was altered to lower the T_g . This change serves several purposes. First, lowering the T_g lowers the melt viscosity without a significant impact on bulk mechanical strength, provided the glass transition temperature remains greater than ambient temperatures. Second, a reduced T_g aids the microencapsulation process by reducing the heat loads on the system. Third, a lower T_g decreases SLS processing time by reducing powder bed temperature biasing requirements. Lastly, a lower T_g reduces the extent of part distortion due to curling caused by thermal history events.

A polymer binder with $T_g \sim 60^\circ\text{C}$ was specified. Using copolymer composition equations derived by Vail,¹³ the new copolymer composition was estimated to be 35/65 wt./wt. MMA/*n*BMA. A sample batch was prepared and the T_g determined by differential scanning calorimetry (DSC). A T_g of 55.5°C was determined by the midpoint method (ASTM D3418).

A series of polymers with various molecular weights were prepared to establish the polymer working curve, which expresses the polymer melt flow viscosity (M.I.) as a function of the polymerization conditions and is defined as follows:

$$M.I. = K \left(\frac{[S]}{[M]} \right)^a \quad \text{Eq. 2}$$

where $[S]$ is the molar concentration of chain transfer agent (a molecular weight control component), $[M]$ the molar concentration of monomer, and K and a are constants specific to the system. The constants were determined using polymers prepared according to table 1. Samples of the resulting emulsion polymers were dried to a film at ambient conditions then dried to constant weight in a convection oven at 40°C. The dried polymers were molded into tensile specimens 3"x0.5"x0.125" using a machined aluminum mold and a Wabash compression molder at conditions of 30,000lbs on an 8"x8" platen area. Tensile specimens were tested for three-point flexural strength (ASTM D638) using a Sintech 1/S mechanical test frame and load rate of 0.5in./min. Molded polymer samples were tested for melt flow viscosity (ASTM D1238) using a Kayness Capillary Rheometer at 200°C and 75psi extrusion pressure. Melt flow viscosity (M.I.) was reported as g/10min.

Figure 12 shows the results of melt flow data for the polymer series specified in table 1. The resulting working curve is given by:

$$M.I. = 273.9 \times 10^6 \left(\frac{[S]}{[M]} \right)^{2.696} \quad [=] \frac{g}{10\text{min}} \quad \text{Eq. 3}$$

Table 1. Polymer synthesis.

Sample	$[S]/[M] (\times 10^3)$
1	0.5
2	1.0
3	2.0
4	3.0
5	4.0

The working curve was verified by preparing a polymer with an expected melt flow index of 15.0g/10min. The resulting melt flow index was 21.3 ± 0.7 g/10min, in good agreement with the expected value.

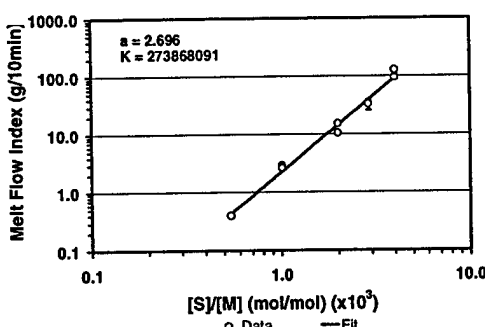


Figure 12. Polymer melt flow viscosity as a function of synthesis parameters.

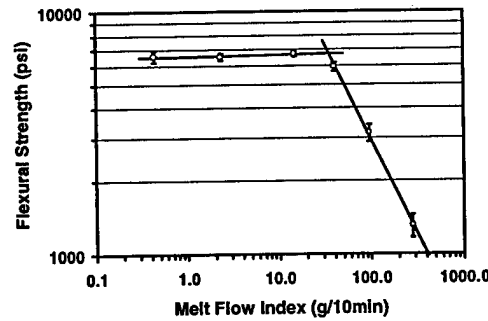


Figure 13. Polymer bulk tensile strength as function of melt flow viscosity.

Figure 13 shows the polymer flexural strength as a function of the melt flow viscosity. Recall that melt flow increases with decreasing molecular weight; therefore, bulk mechanical strength will decrease with increasing melt flow viscosity. This trend is confirmed by the data. Bulk mechanical strength is constant at about 6700psi (46MPa) up to a melt flow viscosity of about 35g/10min, after which the bulk mechanical strength falls precipitously. Melt flow viscosities greater than about 1g/10min have been determined to be optimal for selective laser sintering.¹³ The minimum range is well within the bulk strength plateau for the present polymer system. Indeed, the melt flow can be

increased considerably with little compromise to bulk mechanical strength. Mechanical strength measurements of the verification polymer discussed for the working curve above indicated a flexural strength of 7100 ± 200 psi (49.0 ± 1.4 MPa).

Powder encapsulation was studied using the fluidized bed process. This encapsulation method is different from the spray drying method used in the phase I effort. Impetus for the encapsulation method change is summarized in table 2. The primary reasons for switching methods are the ability to handle large particle systems and the ability to produce discrete uniformly coated particles.

Table 2. Comparison of advantages and disadvantages of spray drying and fluidized bed as microencapsulation processes for selective laser sintering powder feed stocks.

	Pro	Con
Spray Drying	<ul style="list-style-type: none"> • Free flowing powder • Agglomerates + fines • Dispersed coating • Continuous process • Garbage-In / Garbage-Out 	<ul style="list-style-type: none"> • Agglomerates • Small particle limited • Feed preparation
Fluidized Bed	<ul style="list-style-type: none"> • Free flowing powder • Discrete particles • Uniform coating • No feed preparation • Garbage-In / Garbage-Out 	<ul style="list-style-type: none"> • Large particle limited • Batch process

Fluidized bed microencapsulation was initially characterized using spheroidized soda-lime glass as a standard substrate material. Such standard materials provide uniform particle shape and precise control of particle size distribution, thus minimizing contributing effects to microencapsulation results. Emulsion polymers prepared in the binder development task were used as encapsulation media. The primary variables studied were the coating process variables of temperature, fluidization conditions and coating media flow rate, substrate particle size, coating efficiency, coating thickness, and polymer type.

A series of trials were conducted over a three day period during an onsite visit to Applied Chemical Technology, Inc. (Florence, Ala.), a manufacturer of fluidized bed systems and other industrial powder processing equipment. The trials conducted and their coating efficiency results are summarized in table 3.

The encapsulation trials were conducted using a benchtop fluidized bed unit with capacity of about two liters of powder. A heated air stream was introduced into the fluidization chamber to provide simple powder fluidization and, after temperature equilibration, coating media was introduced into the chamber through a downward pointing atomization nozzle. It was prudent to equilibrate operating conditions using water and, without interrupting fluid flow, begin introduction of the coating media to the fluidization chamber. The coating media were approximately 20% wt. solids. Coating media with more than 20% wt. solids repeatedly clogged the atomization nozzle. To further prevent clogging of the atomization nozzle, the dilute emulsions were filtered through a 400mesh

(37 μm) stainless steel screen. Typical encapsulation operating conditions are summarized in table 4.

Table 3. Summary of microencapsulation experiments

Run	Substrate		Coating Type*	Coating Content (vol. %)		
	Type	Size (μm)		Expected	Measured	Efficiency
1	Glass	+45-63	P0	20	16.6	83.0
2			P1	20	16.1	80.5
3			P2	20	18.1	90.5
4			P4	20	17.6	88.0
5			P6	20	16.6	83.0
6			P2	10	8.8	88.0
7			P2	30	25.6	85.3
8			P2	40	34.6	86.5
9	CaP	+75-90	P2	20	16.1	80.5
10		+106-125	P2	20	9.8	49.0
11		+45-63	P2	20	16.2	81.0
12	CaP	+45-63	P2	40	37.0	92.5
13		+106-125	P2	20	11.7	58.8
14		+106-125	P2	40	22.3	55.8

* Increasing n corresponds to increasing melt flow viscosity.

Table 4. Fluidized bed microencapsulation operating conditions.

Temperature (°F [°C])		Fluidization (fpm)	Atomization (psi)	Fluid Flow (g/min)
Inlet	Outlet			
160 [70]	90 [32]	120 – 180	10 – 12	~10

The product materials were analyzed for polymer content using thermogravimetric analysis (TGA). The coating morphology was examined using SEM. And, the particle size distributions of the uncoated and coated powders were determined by laser diffraction.

Polymer content analysis was summarized in table 3. Examination of the data show a dependency on the substrate particle size. Coating efficiencies were generally greater than 80% for particle substrates smaller than about 75 μm in diameter. Coating efficiencies were only about 50-60% for particles substrates larger than about 75 μm in diameter. This discrepancy was attributed to the fluidization method in that simple fluidization of large particles was insufficient to bring the particles into prolonged contact with the atomized coating media. Two repeat experiments were conducted to verify this hypothesis. In both cases, powder fluidization was altered using a Wurster insert, which serves to introduce a directed circulating flow pattern to the powder. In the first experiment, the coating media was directed downward (as in the initial trials) into the directed powder flow. In the second experiment, the coating media was directed co-current from below with the directed powder flow. Results showed the Würster insert improved overall encapsulation efficiency. However, the co-current flow condition provided the best improvement with greater than 80% encapsulation efficiency versus about 60% for the counter-current case.

Particle size analysis coupled with microscopy showed uniform encapsulation of particles by the polymer (figures 14 and 15). Particle size distributions showed consistent shifts to larger particle sizes over the entire

distribution with no significant broadening of the distribution (figure 16). This is indicative of little to no agglomeration of the powder during encapsulation, which was further confirmed by SEM. Particle size shifts were consistent with the expected coating thickness calculated from actual polymer content analysis data (figure 17).

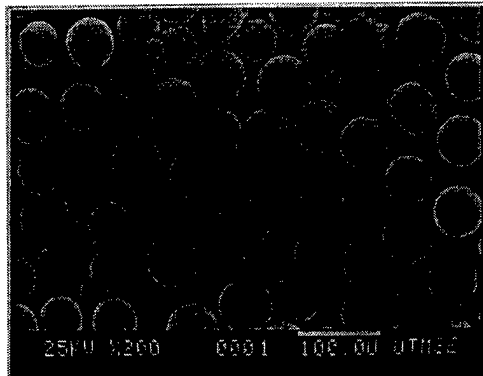


Figure 14. Scanning electron micrograph of soda-lime glass substrate, +45-63 μm particle size distribution.

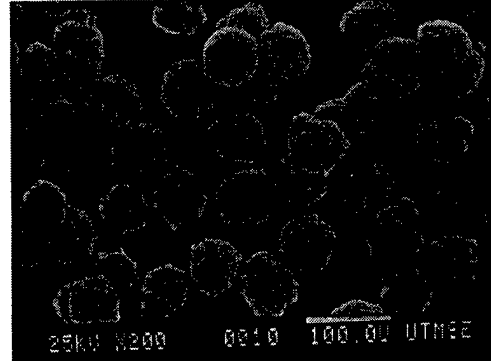


Figure 15. Scanning electron micrograph of polymer encapsulated soda-lime glass, 20% vol.

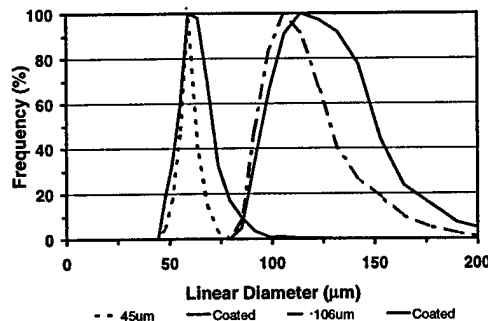


Figure 16. Particle size distributions of coated and uncoated soda-lime glass substrates.

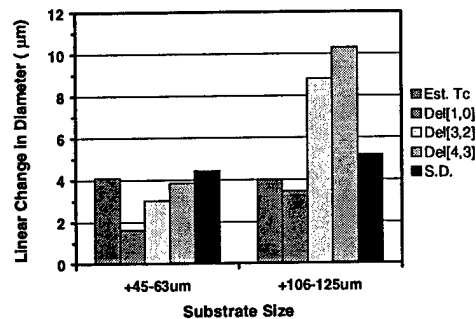


Figure 17. Changes in linear dimension for the various PSD means. T_c – estimated coating thickness, [1,0] – number average mean, [3,2] - volume average mean, [4,3] – weighted average mean, S.D. – standard deviation.

Encapsulation results indicate particle shape has little effect on performance of the coating process. Calcium phosphate powders, which are very irregular in shape and have broad particle size distributions, showed similar encapsulation efficiencies to spherical glass powders of similar particle size fraction. Particle size analysis showed similar shifts in particle size as in the glass powders (figure 18). However, there was indication of particle fines removal due either to agglomeration to larger particles or to material loss. Subsequent trials resulted in coating efficiencies of about 80% for +106-125 μm powder fractions while +45-63 μm powder fractions showed greater than 100% coating efficiencies, clearly indicative of loss of material fines. Microscopy confirmed elimination of fines and the presence of some agglomerates; however, the nature of the polymer coating was difficult to discern as compared to the spherical glass materials.

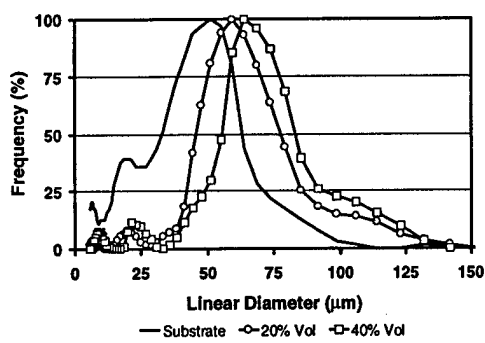


Figure 18. Particle size distributions of uncoated and coated calcium phosphate powders. Note diminished fines peak and uniform shifts with increasing polymer content.

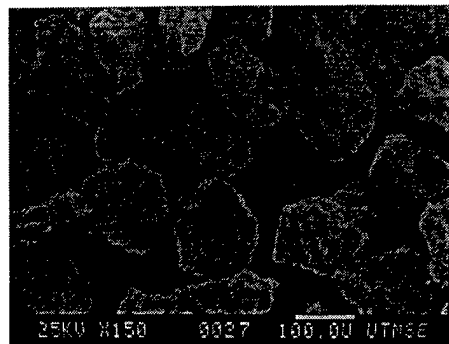


Figure 19. Scanning electron micrograph of polymer coated calcium phosphate. Note lack of fines compared to figure 11.

SLS processing parameters were determined using a SinterStation® 2000 commercial selective laser sintering platform (DTM Corporation, Austin, Texas). Critical process variables considered were scanning parameters, process parameters, and material scaling parameters.

SLS scanning parameters are the laser power (P), laser beam speed (bs), spacing between adjacent scan vectors ($scsp$), and the focused laser beam spot radius (ω). The first three parameters are commonly lumped into applied energy density quantity given as:

$$EnergyDensity = \frac{kP}{bs * scsp} [=] \frac{cal}{cm^2} \quad \text{Eq. 4}$$

where k is a constant for unit conversion. The parameter $scsp$ is constrained by the laser beam spot radius, ω , in that $scsp$ must be smaller than ω to ensure laser beam overlap of adjacent scan vectors.

The process variables are the layer thickness (L_t) and the powder temperatures. The layer thickness is governed by the powder particle size and is generally 2-4 times the powder particle size. Too thin layers will cause particle binding between the powder application roller and previously sintered layers, typically leading to movement of the sintered part and severe dimensional distortion. Too thick layers lead to poor geometric resolution and limit powder performance due to increased thermal transport resistance. Powder bed temperature is important to ensure optimal material performance and good part quality. The powder bed temperature is normally biased near the material softening point to minimize both the applied energy density and the extent of curl that can occur in a sintered layer due to large thermal gradients. Generally, encapsulated powders do not experience curl, provided the glass transition temperature is lower than about 100°C. However, it is still advisable to bias the temperature of encapsulated powders to optimize material performance for two reasons: 1) parts produced from temperature biased materials will be stronger since more of the applied laser energy is converted to activating the binder, and; 2) lower applied laser energies are required, which simultaneously reduce the

extent of polymer binder degradation during SLS fabrication. Binder degradation is a competing process to strength development in SLS processing of polymer encapsulated systems. Both effects mentioned are quantifiable phenomena.

The scaling parameters consider material shrinkage and the finite size of the scanning laser beam. Consequently, process scaling parameters are material as well as machine dependent.

Processing parameters were determined using a standard material designated CP-001. This material was comprised of the standard calcium phosphate substrate with composition Ca/P=0.9. The substrate particle size was +106-125 μ m. Fifteen kilograms of this powder was prepared. Ten kilograms were encapsulated with an emulsion polymer having a melt flow viscosity of 21.3 \pm 0.7g/10min at 200°C and 75psi and a glass transition temperature of 55°C. Five of the ten kilograms were encapsulated with 20% vol. (8.87% wt.) coating and the remaining five kilograms were encapsulated with 30% vol. (14.22% wt.) polymer. These separate batches were prepared to further evaluate the encapsulation process. The resulting encapsulated powders had polymer contents of 17.4% vol. (7.52% wt., 84.8% yield) and 26.0% vol. (11.95% wt., 84.0% yield), respectively. The two batches were mixed to produce a homogenous powder with 21.7% vol. (967% wt.) polymer. Uncoated powder in the amount of 0.09g/g encapsulated powder was added to the encapsulated powder mixture to obtain 20% vol. (8.87% wt.) polymer content.

Powders are normally prepared in a manner similar to that described above; however, they are prepared from a single encapsulated source material. The purpose of preparing powders in this manner is two fold. First, the preparation method provides precise control of the polymer composition. This is necessary since the encapsulation process has inherent variance in the coating efficiency. Provided the initial encapsulated powder polymer content is not significantly different than the required polymer content, the performance of the final material will not be significantly affected. Generally, the initial encapsulated powder is formulated to obtain 5-10% excess polymer content with respect to the final polymer content. Second, the addition of unencapsulated substrate powder is beneficial to subsequent post-processing steps, in that it provides free surfaces for later attachment of post-processing materials. Recall that the polymer binder is a fugitive material.

SLS process parameters were determined using visual inspection methods and a one inch square scan test pattern. Several single layer scans of the test pattern were created using a range of applied energy densities to qualitatively determine a good scanning parameter set, where a good set corresponded to being able to remove a contiguous single layer from the powder bed. An applied energy density of 2.0cal/cm² was used subsequently to determine powder layer thickness and powder bed temperatures.

Powder layer thickness was determined by repeatedly scanning the one inch square test pattern and applying a new layer of powder. If movement of the scanned pattern was observed, then the layer thickness was increased by 0.001in. (25.4 μ m) and the test repeated. The minimum layer thickness was determined to be 0.008" (203 μ m). The test pattern was scanned for twenty successive layers

using the determined layer thickness and no movement nor distortion of the part was observed.

Powder bed temperatures were determined by assessing the breakout quality of 0.5inch depth of the scan test pattern. It is necessary to fabricate an object because scanning adds energy to the system. The scanned object is essentially a dense heat source surrounded by an insulating powder. If the powder bed temperature is biased too high, then heat conduction from the sintered object will cause local surface growth of the object over time. If many objects are present in the powder bed, then gradual sintering of the bed may occur. This results in inaccurate parts as well as difficult part breakout and reduced recycleability of the powder. In the present case, a powder bed temperature of 62°C was determined to be sufficient. This value is higher than the glass transition of the polymer coating. The discrepancy is probably due to the infrared sensor, which is sensitive to material emissivity.

SLS scanning parameters were quantified with flexural strength of three-point bend specimens fabricated using various applied energy densities. Two sets of three-point bend specimens measuring 0.5in. x 3in. x 0.25in. were fabricated. The first set was oriented with the long specimen axis parallel to the laser fast axis (*x*-axis of the powder bed). The second set was oriented with the long specimen axis perpendicular to laser fast axis (figure 20). Each set was fabricated using applied energy densities in the range 0.5-3.0cal/cm². Three specimens were fabricated for each energy density value. The applied energy density parameters *bs* and *s_{csp}* were held constant at 75ips and 0.004in., respectively. Laser power ranged from 3.0-18.0W. Mass and dimensions were measured for each specimen. Flexural strength was determined with an Sintech 1/S mechanical test frame equipped with a calibrated 50lb load cell. Strain rate was 0.5in/min.

Figure 21 shows a linear development of green strength with increasing applied energy density. The maximum observed strength was about 200psi (1.4MPa). Generally, as the applied energy density is increased, polymer degradation begins to dominate resulting in a strength plateau and an eventual strength decrease. This behavior was not observed, indicating the applied energy density could be increased to achieve greater green strength for this particular geometry. Figure 21 shows the discrepancy in three-point bend strength between the two sets of specimens. Specimens oriented along the *y*-axis (short axis scan) are stronger for a given applied energy density than specimens oriented along the *x*-axis (long axis scan). This phenomena has been shown to be a result of differences in the average temperature of the scanned area.¹³ That is, short vector lengths will produce a higher average temperature of the scanned area and, therefore, more viscous flow of the polymer. On the other hand, higher temperatures will cause polymer degradation as well. Figure 22 shows the compressive strength of cylindrical specimens measuring 0.35in. in diameter by

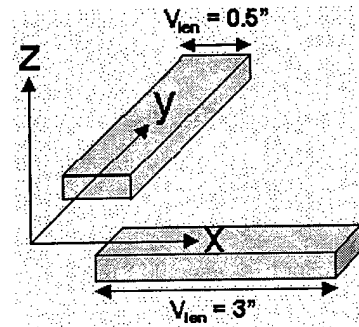


Figure 20. Strength specimen orientations with respect to fast scan *x*-axis.

0.35in. tall. These parts are of uniform cross-sectional area and do not show a dependence on orientation with respect to the laser scan direction. However, due to their small cross-sectional area, strength does appear to reach a maximum plateau value, indicating polymer degradation is beginning to dominate at the higher applied energy density levels.

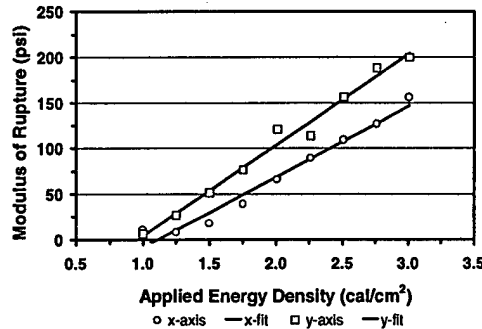


Figure 21. Three-point bend strengths with applied energy density. Curves show dependence of strength development on part orientation with respect to scanning axis.

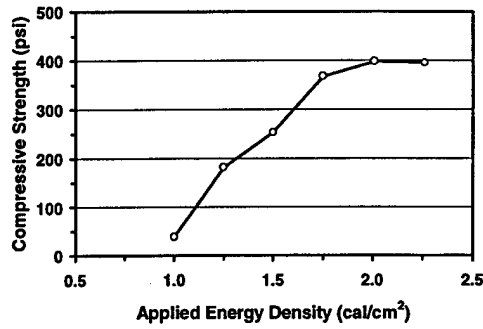


Figure 22. Compressive strength of cylindrical specimens with applied energy density.

Material scaling parameters were determined using three-point bend specimens with measurements ranging in size from 0.25in. x 1.0in. x 0.125in. to 0.5in. x 3.0in. x 0.25in. Two sets, oriented orthogonally, were fabricated using a constant applied energy density of 2.0cal/cm². Mass and dimensions were measured for each specimen. Scaling parameters were calculated by linear least squares fit of the measured dimensional deviation, $\Delta\ell$, versus the nominal dimension, ℓ . The slope of this regression fit is the material shrinkage, $\Delta\ell/\ell$, and the intercept is related to the radius of the laser beam.

Figure 23 shows the calculated shrinkages in the x - and y -directions to be very similar at 0.58% and 0.51%, respectively. However, laser beam size compensation is greater in the x -direction than in the y -direction (283 μ m vs. 154 μ m). The difference is probably due to scan vector blooming along the fast scan x -axis, which results from changes in laser beam velocity near the scan vector endpoints. The endpoints appear as teardrops and the net result is a sintered vector that is too long. The resulting compensation value for the x -direction encompasses not only the laser beam radius, but also vector endpoint growth due to blooming. In the y -direction (perpendicular to the scan vector), the resulting compensation value corresponds only to the laser beam radius. Profilometry of the laser beam showed a beam radius of 195 μ m, consistent with compensation results.

The vector blooming phenomena is inherent to early versions of commercial SLS platforms. Newer platforms, beginning with the SinterStation® 2500, implement hardware and software modifications that modulate laser powder to compensate for laser beam velocity changes at vector endpoints.

The calculated material shrinkage and beam compensation do not differ significantly ($p=0.005$) between specimens fabricated using an applied energy density of 2.0cal/cm² and specimens fabricated with applied energy densities in

the range $0.5\text{-}3.0\text{cal/cm}^2$. Verification of the process scaling parameters yielded parts with average nominal deviations of $-54.0\pm83.1\mu\text{m}$, consistent with the material particle size (figure 24). This deviation corresponds to the inherent dimensional noise for the given material system and scaling parameters.

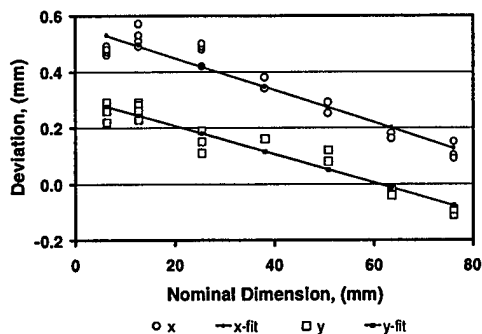


Figure 23. Material shrinkage calibration for $+106\text{-}125\mu\text{m}$ polymer encapsulated powder (20% vol.) scanned at an applied energy density of 2.0cal/cm^2 . Layer thickness = $0.008"$ ($203\mu\text{m}$), bed temperature = 62°C .

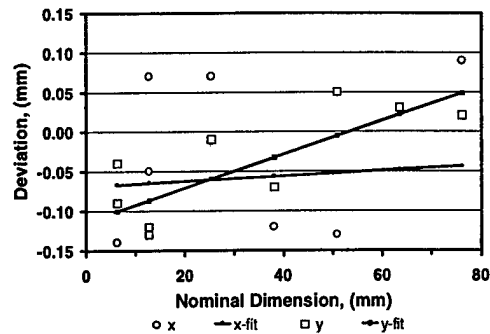


Figure 24. Material shrinkage calibration verification data.

To date, the CP-001 material has been recycled through the machine a total of eight times and resifted four times. The polymer composition has dropped 1.6% to 8.73% wt. (19.82% vol). This change is not significant, but it is important to track material composition to ensure reproducible part fabrication. There is no indication to the material morphology nor how the polymer properties may be changing with continued use.

Post-processing of SLS fabricated green parts is illustrated in Figure 25. First, the part is infiltrated with a suitable liquid and then dried to constant weight. The dried part is then heat treated to sinter the calcium phosphate particles. The infiltration-dry-sinter sequence may be repeated to achieve desired part properties. Five physical changes occur during post-processing: 1) the polymer binder thermally decomposes and volatilizes from the fabricated object (first heat treatment cycle only); 2) the calcium phosphate composition (Ca/P) may be modified; 3) dimensional changes may occur; 4) porosity may be altered; and 5) mechanical strength may be altered. Each of these changes must be quantified to determine an optimal processing window and to ensure final part performance.

The infiltration step is used to deposit material into the porous part, which is thought to serve three purposes: 1) it provides control of the calcium phosphate composition; 2) it provides control of the microstructure; and 3) it reduces shrinkage of the fabricated object. Compositional control is accomplished using an infiltrating liquid containing a material that will alter the overall Ca/P ratio of the object material. Changes to the Ca/P ratio modifies material chemistry and mechanical properties. The added material increases the part density, which should reduce shrinkage during heat treatment.

Key aspects of the infiltration process are the composition of the infiltrating solution and the completeness of infiltration. Typical solutions are aqueous based calcium phosphates of composition $\text{Ca/P}\sim 0$. The phosphate

constituent is typically derived from orthophosphoric acid (H_3PO_4 , 85% wt. stock), although other phosphate sources are possible, such as water soluble orthophosphoric acid salts.

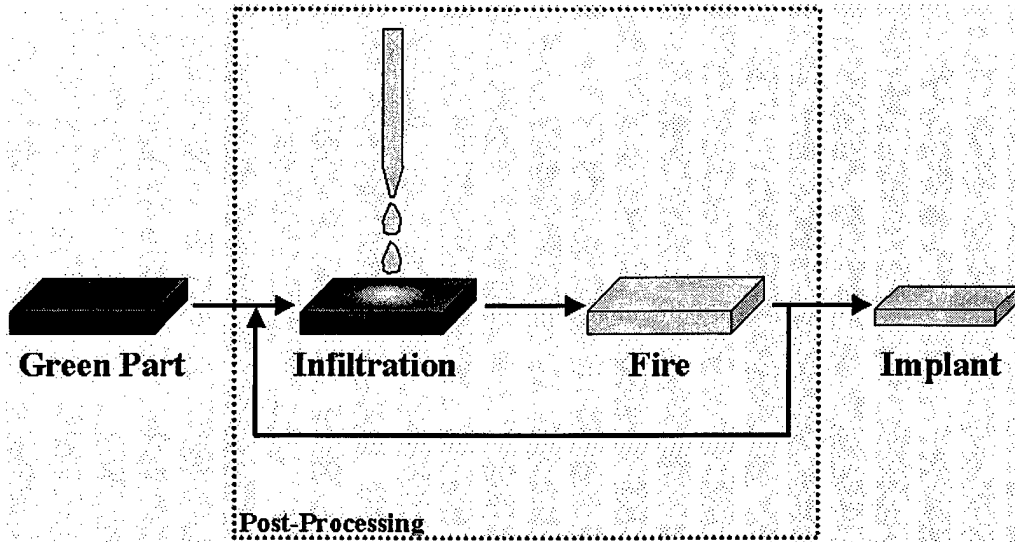


Figure 25. Post-processing process schematic.

Solution formulation was driven by performance during infiltration trials. Aqueous solutions of 3, 6, 12, 16% wt. P_2O_5 ($Ca/P=0$) were used in the trials. Cylindrical specimens 0.3in. diameter by 0.3in. height were molded from the CP-001 material discussed earlier. Molded specimens had a porosity of about 50%, consistent with the porosity of SLS fabricated objects. Infiltration performance was determined qualitatively by observing the extent of liquid penetration into the porous samples. Liquid fronts were easily discernable, although an aqueous based dye will aid visualization. The extent of liquid penetration could be determined visually by sectioning the sample. The extent of liquid penetration was also quantified by material balance as follows:

$$\begin{aligned}
 V_s &= \frac{\pi d^2 h}{4} ; \quad V_l = \frac{m_w - m_d}{\rho_l} \\
 \rho_s &= \frac{m_d}{V_s} ; \quad \rho_t = \frac{x_p / \rho_p}{x_p / \rho_p + (1-x_p) / \rho_c} \\
 \varepsilon_t &= 1 - \frac{\rho_s}{\rho_t} ; \quad \varepsilon_a = \frac{V_l}{V_s} \\
 \%error &= \frac{\varepsilon_t - \varepsilon_a}{\varepsilon_t}
 \end{aligned} \tag{Eq. 5}$$

where V_s is the sample volume, V_l the liquid volume, ρ_s the sample density, ρ_t the theoretical sample density, ε_t the theoretical porosity, ε_a the actual porosity, d the sample diameter, h the sample height, m_w the wet sample mass, m_d the dry sample mass, ρ_l the liquid density at experimental conditions, x_p the polymer mass

fraction of the sample, ρ_p the polymer density, and ρ_c the ceramic density. An error of less than 5% was considered to represent complete infiltration.

Aqueous solutions did not effectively infiltrate the samples due high liquid surface tension, although low P_2O_5 content solutions performed better. Infiltrating performance was greatly improved by the addition of 0.5% wt. of the anionic surfactant sodium dodecyl sulfate (SDS). However, complete infiltration was not repeatable and also appeared to be time dependent. Solution formulation was altered to include methanol (MeOH) to further reduce the solution surface tension. Solutions containing 50/50 wt/wt MeOH/ H_2O proved excellent infiltrating solutions at all P_2O_5 concentrations.

Infiltration trials provided determination of preferred infiltrating methods, of which two produced repeatable results. The first method consists of placing a quantity of solution in a shallow pan then placing the sample in the solution. The liquid level in the pan should be low to avoid complete immersion of the sample as this inhibits liquid penetration. Liquid penetration was followed visually. On completion, the sample was dabbed lightly on a paper towel to remove excess surface liquid. The extent of infiltration was sample size dependent and, therefore, time dependent. Effects of immersion time were not studied. The second method involves placing the specimen on a paper towel and slowly dripping liquid onto the surface of the specimen until bleedthrough occurs at the paper towel. At this point, the sample is inverted and placed at a dry location and the process repeated. The sequence is repeated 2-3 times to ensure complete wetting of the sample. The sample is then placed on a wax sheet and liquid dripped on the surface until it is visible at the wax paper surface. At this point, the part is saturated. This method is fast and very repeatable and most samples were infiltrated in this manner.

In subsequent post-processing work, the two infiltration methods discussed above were found to be more or less suitable depending on the state of the sample. For example, the first method, involving liquid uptake by simple capillary action, proved more suitable for samples that had been through one heat treatment. That is, samples free of the polymer binder infiltrated better. The second method, involving liquid addition from the surface, proved more suitable for samples containing polymer binder. This reflects the low surface energy of polymers, which are not easily wetted by most liquids. As such, the driving force for liquid uptake is low. The second infiltration method increases the liquid penetration driving force through both gravity and the use of the dry paper towel. Once the polymer is removed, the high energy ceramic surface is more conducive to liquid wetting leading to fast liquid uptake by partial immersion in a liquid source.

Following infiltration, saturated parts were dried to constant weight prior to heat treatment. Drying of saturated porous media of this type has been studied extensively by Vail, *et al.*,¹⁴ who found it to be a critical step in the post-processing sequence. Key aspects of the drying process are the drying rate, solids content of the infiltrating liquid, object shape, and initial strength of the porous component. Generally, control of the drying rate is most critical with slower

drying rates required during the initial stages to prevent both profound solids migration and catastrophic failure of the dried object.

In the present work, drying physics were not studied. However, drying conditions were controlled with the aid of a sealed chamber and saturated salt solutions to control relative humidity. Humidity was controlled using a saturated sodium chloride (NaCl) solution, which produces a relative humidity of $70\pm2\%$ at STP.¹⁵ The high R.H. favors slow drying rates, but does not guarantee a slow rate, since mass and heat transfer mechanisms are geometry dependent. However, all the samples studied in this work were of consistent volume and geometry, thereby ensuring to some extent drying uniformity. Samples dried in this manner were 80-95% dry after a period of twelve hours at the stated conditions. The extent of drying is linear with decreasing P_2O_5 content of the infiltrating solution (figure 26). Samples dried further in a convection oven for two hours at $40^\circ C$ were 95-98% dry. The second drying step is also linear with decreasing P_2O_5 content of the infiltrating solution.

Heat treatment studies were conducted to determine optimal firing conditions, to determine optimal infiltrating solution composition, and to quantify resulting material properties. These considerations have important constraints, namely: 1) the final material composition; 2) dimensional control; 3) mechanical strength, and 4) porosity. As discussed earlier, the initial Ca/P ratio of the substrate powder is 0.9. The target Ca/P ratio is preferred to be ~ 0.55 . This compositional change can be achieved with a single infiltration step as shown by material balance; however, such a large change may incur large dimensional change and associated geometric distortion. Dimensional shrinkage must be minimized to ensure geometric accuracy. Dimensional changes of only a few percent are preferred as they tend to be linear with object size. Mechanical strength should be high to ensure durability, although mechanical properties consistent with normal bone are preferred. Heat treatment affects mechanical strength and dimensional accuracy. Material composition and heat treatment affect mechanical strength.

The principle variables studied were heat treatment temperature, heat treatment time, and infiltrating solution composition (or final material composition). Heat treatment temperatures were 750° , 800° , and $850^\circ C$. Heat treatment times were 0.5, 1.0, and 2.0 hours. The firing cycle profile is shown in figure 27. The infiltration solutions had compositions 6, 12, and 16% wt. P_2O_5 . Cylindrical compression test specimens 0.35in. diameter by 0.35in. height were fabricated via SLS using an applied energy density of $2.0\text{cal}/\text{cm}^2$. These specimens incorporated measurement markers to ensure data acquisition

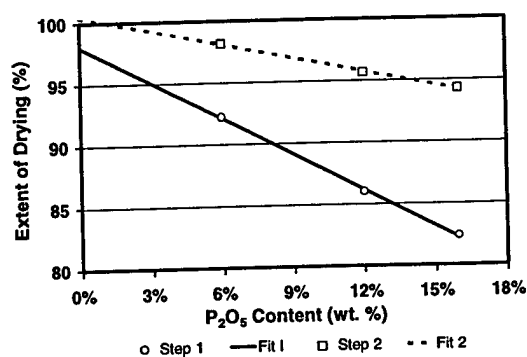


Figure 26. Extent of drying for humidity controlled conditions (step 1) and, subsequently, rigorous conditions (step 2).

consistency (figure 28). The SLS fabricated green specimens had compressive strengths of about 400psi (2.8MPa, figure 22). Compressive strength was determined using Sintech 1/S mechanical test frame equipped with a calibrated 1000lb load cell and a strain rate of 0.5in/min. Dimensional and mass measurements were obtained for shrinkage and material balances, respectively. Material balances were calculated using the following formulas:

$$\begin{aligned}
 m_u &= m_d - m_s \\
 \Delta m_{est} &= m_d - m_f \\
 \Delta m_t &= m_s x_{p,s} + m_u x_{SDS,u} + (m_u - m_l x_{s,l}) \\
 x_{P_2O_5,s} &= \frac{FW_{P_2O_5}}{2\left(\frac{Ca}{P}\right)_s FW_{CaO} + FW_{P_2O_5}} \\
 \left(\frac{Ca}{P}\right)_{est} &= \frac{m_s(1-x_{p,s})x_{CaO,s}}{m_s(1-x_{p,s})x_{P_2O_5,s} + m_u x_{P_2O_5,u}} \frac{FW_{P_2O_5}}{FW_{CaO}} \frac{1}{2} \\
 \left(\frac{Ca}{P}\right)_t &= \frac{m_s(1-x_{p,s})x_{CaO,s}}{m_s(1-x_{p,s})x_{P_2O_5,s} + m_l x_{P_2O_5,l}} \frac{FW_{P_2O_5}}{FW_{CaO}} \frac{1}{2}
 \end{aligned} \tag{Eq. 6}$$

where Δm_{est} is the calculated mass change after heat treatment, Δm_t the theoretical mass change after heat treatment, Ca/P the calcium phosphate composition, m_s the initial sample mass, m_d the dry sample mass, m_l the mass of liquid uptake, m_u the mass of solid uptake after drying, m_f the heat treated sample mass, $x_{i,j}$ the mass fraction of the i -th component in the j -th species, FW_i the formula weight of the i -th species, s refers to the sample, u refers to the uptake, l refers to the infiltration liquid, t refers to the theoretical value, and *est* is the estimated value. Initial polymer content of the SLS fabricated specimens, $x_{p,s}$, was typically 8.1% wt. (18.6% vol.), as determined by thermogravimetric analysis.

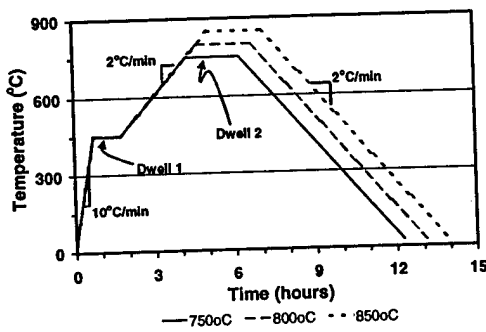


Figure 27. Firing cycle profiles.

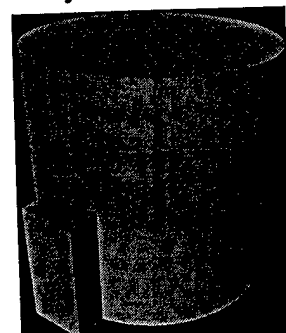


Figure 28. SLS fabricated compression test specimen configuration. Dimensions: 0.35in. diameter by 0.35in. tall.

Dimensional analysis of SLS fabricated test specimens indicated the measurement marker on each test specimen constituted $1.89 \pm 0.13\%$ of the total volume of the specimen, well within an acceptable total cumulative measurement error of 5% for volumetric properties. The displacement porosity of the samples, determined by material balance of the infiltrating liquid uptake, was $47.6 \pm 1.5\%$ ($n=163$). The estimated displacement porosity did not differ statistically between

the different infiltrating solutions ($p=0.005$, $n_1=n_2=25$, $n_3=113$). The error between the displacement porosity and the volumetric porosity was $-3.9\pm3.1\%$, in excellent agreement. Solid uptake of the specimens ranged from 4-12% of the sample mass and was linear with the solids content of the infiltrating solution (figure 29). Material balances showed the error in measured mass change due to polymer degradation was $1.54\pm1.99\%$ ($n=99$).

Although there was no statistical difference in the measured mass loss corresponding to either P_2O_5 uptake or heat treatment conditions ($p=0.005$), the heat treated sample color could be visually correlated to P_2O_5 uptake and sintering temperature. Increasing P_2O_5 uptake produced more gray samples while increasing sintering temperature produced more white samples. Clearly the deposited P_2O_5 is affecting the polymer binder decomposition. It is well known that phosphorous compounds serve as flame retardants in polymer systems.¹⁶

Figure 30 shows the compressive strength and modulus for samples sintered 60 minutes at $800^\circ C$. There is a strong dependence of the compressive behavior on the phosphorous pentoxide (P_2O_5) uptake of the porous specimen. This suggests two possible mechanisms for strength development in this system: 1) the deposited P_2O_5 is aiding sintering of the porous network or 2) the compressive strength is related to the ultimate part density. There is strong indication that both mechanisms are contributing.

Figure 31 shows the dimensional shrinkage increases with the P_2O_5 uptake, suggesting P_2O_5 is acting as a sintering aid. That is, during heat treatment, the deposited P_2O_5 alloys with substrate particle surfaces to lower the local Ca/P ratio. According to the CaO- P_2O_5 phase diagram, this compositional change reduces the local material melting point.¹⁷ Local melting point depression induces liquid phase sintering, which increases densification and shrinkage. Therefore, contrary to the belief the added P_2O_5 reduces shrinkage by reducing the initial porosity, added P_2O_5 increases densification by inducing liquid phase sintering. Figure 30 also shows shrinkage to be anisotropic in the z-direction and is typically twice the shrinkage as in the xy-plane. The anisotropy is attributable to the stratified nature of the z-axis resulting from SLS fabrication.

Figures 32 and 33, respectively, show that compressive strength and shrinkage behavior were essentially independent of the sintering conditions over the given ranges ($p=0.01$, $30\text{min} \leq t \leq 120\text{min}$, $750^\circ C \leq T \leq 850^\circ C$). These results suggest the final density, which is directly related to material uptake, is the major contributing factor to the strength development of this system at these sintering conditions. Figure 34 shows the dependence of compressive strength of all samples on final part density (or porosity). There is no differentiation in the data between either sintering conditions or the amount of P_2O_5 uptake.

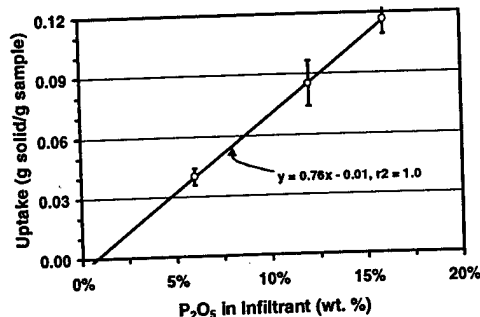


Figure 29. Solid (P_2O_5) uptake as a function of the infiltrating solution composition.

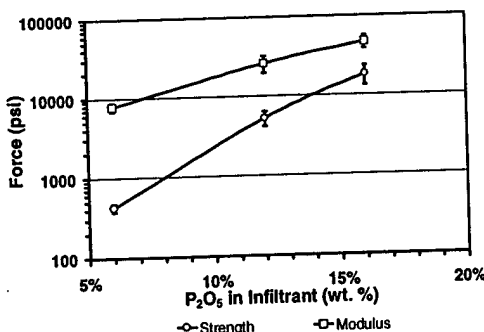


Figure 30. Compressive strength and modulus as a function of infiltrating solution composition. First infiltration step in the post-processing sequence of +106-125 μm polymer coated calcium phosphate SLS green parts. One hour at 800°C.

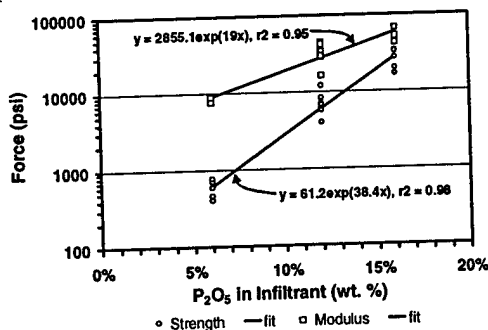


Figure 32. Compressive strengths and moduli of all samples fired over the range 750-850°C for 30-120 minutes as a function of the infiltrating solution composition. First infiltration step in the post-processing sequence of +106-125 μm polymer coated calcium phosphate SLS green parts.

The independence on sintering conditions is contrary to common observance. Generally, as sintering time and sintering temperature increase, densification also increases. The invariance observed here may be a consequence of the inherent particle size of the system, since sintering behavior is a strong function of the particle size. According to most sintering models, the rate of densification is at least inversely proportional to the square of the particle size.¹⁸ Therefore, one would expect similar specimens fabricated from smaller particle size systems to show a

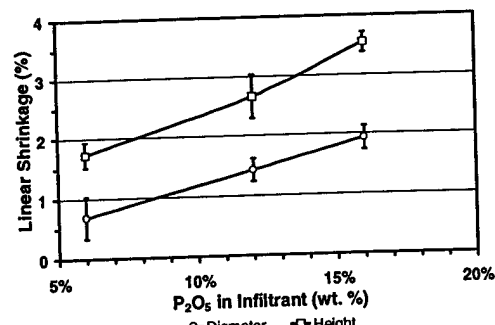


Figure 31. Shrinkage in the xy -plane and z -axis as a function of infiltrating solution composition. First infiltration step in the post-processing sequence of +106-125 μm polymer coated calcium phosphate SLS green parts. One hour at 800°C.

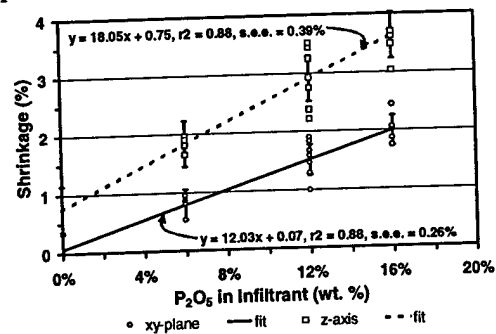


Figure 33. Shrinkages in the xy -plane and z -axis of all samples fired over the range 750-850°C for 30-120 minutes as a function of the infiltrating solution composition. First infiltration step in the post-processing sequence of +106-125 μm polymer coated calcium phosphate SLS green parts.

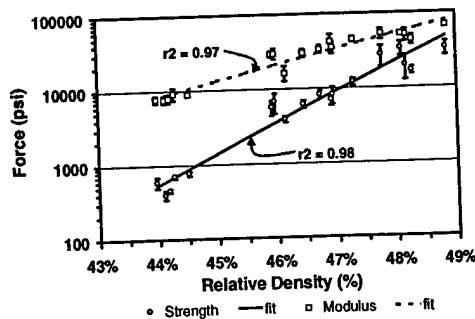


Figure 34. Compressive strengths and moduli as a function of final relative density following heat treatment. First infiltration step in the post-processing sequence of +106-125 μm polymer coated calcium phosphate SLS green parts.

more marked dependence on the sintering conditions.

The preceding discussions indicate to obtain strong parts it is best to achieve a high P_2O_5 uptake. However, increased P_2O_5 uptake increases dimensional shrinkage, leading to an inherent tradeoff between part strength and dimensional accuracy. Maximum shrinkages were $2.0 \pm 0.3\%$ and $3.6 \pm 0.4\%$ in the xy -plane and z -axis, respectively. These are not large shrinkages; however, it is important to recall that additional post-processing sequences may occur and these additional steps will also incur a shrinkage. At the medium P_2O_5 uptake (12% infiltration solution solids) the shrinkages were $1.6 \pm 0.3\%$ and $3.0 \pm 0.5\%$, respectively, roughly 80% of the maximum values. Compressive strengths at these median conditions were $7,000 \pm 1060$ psi (48.3 ± 7.3 MPa) with a modulus of $33,500 \pm 4900$ psi (231.0 ± 33.8 MPa). These values compare well with the compressive strength of cancellous bone. The minimum uptake condition is not recommended, since the compressive strengths were well below 1,000 psi (6.9 MPa).

As shown in Figure 34, heat treated samples had porosities of 51-56%. This corresponds to an average increase in porosity of 12.4% from the initial SLS fabricated green shapes. Considering the average shrinkage incurred during heat treatment, the porosity increase agrees well with the loss of polymer from the system (~20% vol.). The pore size distributions of heat treated samples were determined using mercury porosimetry. Figure 35 shows a typical pore size distribution with a median pore size of $37.1 \mu\text{m}$ and an average pore size of $39.2 \pm 16.9 \mu\text{m}$. These data are very similar to data obtained in the phase I effort using a particle fraction of $+75-106 \mu\text{m}$. In this work, a larger particle size was proposed to increase the pore size. Clearly, this was not the case, and further analysis indicates the measured pore size is consistent with pore size estimates determined from particle packing models.

In the ideal case, consider a cubic packing of regular particles of radius a and packing efficiency 52.4% (equivalent void space diameter is $a/2$). It can be shown from geometry that the minimum interstitial distance between particles of the cell occurs on the cell face and is $2a(\sqrt{2}-1) \approx 0.828a$ (figure 36). The maximum interstitial distance between particles of the cell occurs within the cell and is coplanar with the cell diagonal and the minimum interstitial distance and is $2a\sqrt{4-2\sqrt{2}} \approx 2.165a$. Therefore, for a particle size distribution of $+106-125 \mu\text{m}$, the

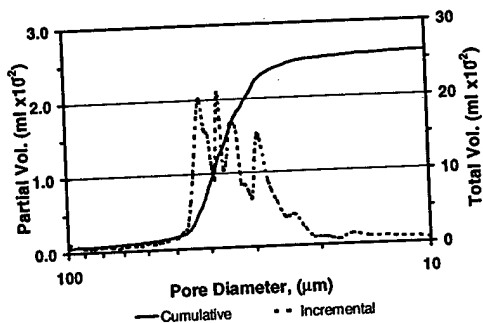


Figure 35. Pore size distribution of calcium phosphate samples following first heat treatment.

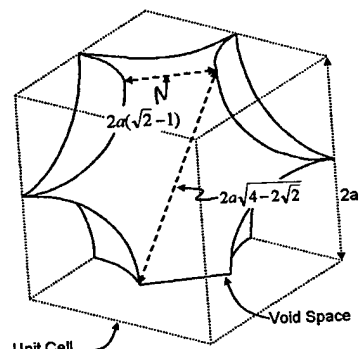


Figure 36. Unit cell configuration.

pore size would be expected to range from 43.9-135 μm . However, the ratio of the minimum to maximum interstitial distance is the same as the cell coordination number, CN, which is six for a cubic cell. That is, the measured pore size will be governed by the minimum interstitial distance. In other terms, access to internal voids, which may be large, will be dominated by flow of material through pores with diameters on the order of the minimum interparticle distance.

Summary of Materials Formulation Tasks

Materials formulation is nearly complete. Raw material synthesis processes have been established and the materials characterization methods and resulting properties have been quantified. Considerable new quantified data have been gathered to ensure fabrication of calcium phosphate objects with consistent material properties and dimensional accuracy. Most of the post-processing steps have been developed and their effects quantified.

Results showed that calcium phosphate powders ($\text{Ca}/\text{P}=0.9$) can be produced in quantity and with specific particle size distributions. These powders can be effectively encapsulated with emulsion based polymers, which can have a wide range of properties, such as melt flow viscosity and glass transition temperature. The fluidized bed encapsulation process can be used to achieve about 80-85% encapsulation efficiency of the calcium phosphate powders. Results showed a calcium phosphate powder of fraction +106-125 μm with a polymer content of 20% vol. (8.87% wt.) was a good starting material for SLS fabrication of green objects.

SLS results showed that green parts could be fabricated using applied energy densities in the range 1-3cal/cm². However, choice of applied energy density should be considered with respect to the object cross-sectional area. Dimensional analysis showed the material scaling parameters were independent of object size and scanning conditions. However, these scaling parameters are specific for the given material, the process conditions, and the given machine. Green parts had tensile and compressive strengths on the order of 200psi and 400psi, respectively, sufficient to permit handling of the objects prior to post-processing methods.

Post-processing results for the initial sequence were very encouraging. Compressive strengths similar to cancellous bone were achieved with controllable shrinkage of the object during heat treatment. High porosity was obtained; however, the average pore size was lower than the optimal 100 μm pore size generally accepted to facilitate tissue ingrowth.

Numerous parts were fabricated in the scope of the materials formulation tasks. Figure 37 shows common geometrical shapes currently used in bone augmentation procedures. These objects demonstrate the capabilities of the technology to produce commodity type implants suitable in application in broad scope of treatments. Figure 38 shows an anatomical shape that demonstrates the more promising potential of this technology to provide custom treatment of bone defects.

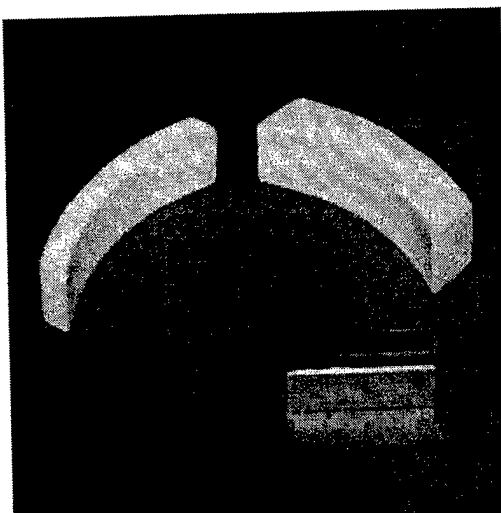


Figure 37. Common implant shapes fabricated by SLS from materials developed in this work. Reference bar is 2.5cm in length.

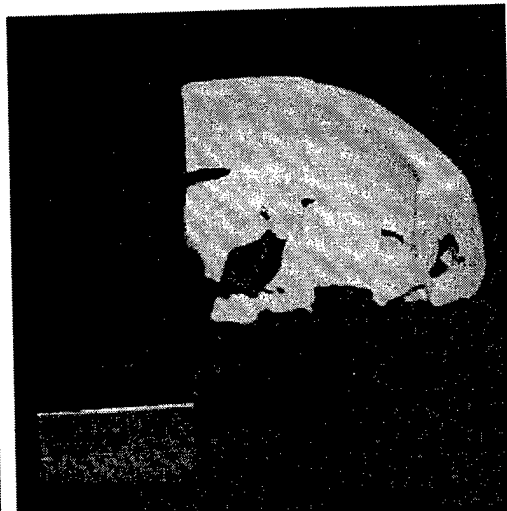


Figure 38. Superior view of the supra orbital. Object fabricated by SLS at $\frac{1}{2}$ scale with data derived from computed tomography using materials developed in this work. Reference bar is 2.5cm in length.

Task Group 4 - Preclinical Evaluation

An implant study in canines, started at the end of the phase I effort, was completed shortly before the start of the phase II effort. Implants for augmentation of alveolar ridge defects in canines were fabricated via SLS. The implants were designed using medial-lateral width and mandibular bone height measurements of study animals and were roughly rectangular in shape and tapered to decrease their medial-lateral width inferiorly or apically (figure 39). The implants incorporated penetrating hexagonal macropores intended to provide increased opportunity for tissue invasion. No macropores intersected the implant crest, thus presenting a solid dome to overlying gingival tissue.

To create skeletal defects, mandibular first molars were removed bilaterally in each of six mongrel canines. Following initial soft tissue healing, the extraction sites were surgically exposed. Using a defect template, sufficient bone was removed to model the severely atrophic alveolar ridge defect. SLS fabricated implants were placed into the defects and primary closure was achieved. Radiographs were obtained every four weeks using custom fabricated positioning stents. Animals were sacrificed for histological analysis at four to twelve months.

Radiographic analysis showed the implants to be infiltrated increasingly with new bone over time (figure 40). Evidence of implant degradation and resorption were noted by changing implant contour, especially in the apical aspects. Clinically, all sites were covered with healthy gingival tissue.

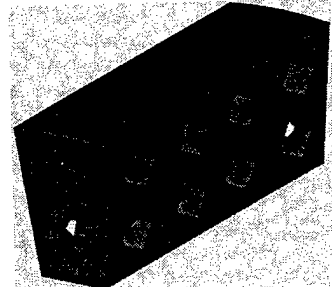


Figure 39. Geometry of alveolar ridge implant used in canine study. Dimensions: $3.3 \times 6.6 \times 15.3 \text{ mm}^3$. Macropores are ~2mm in diameter.

Histologic sections revealed SLS formed implants in intimate contact with host bone. Implants showed excellent biocompatibility and bone ingrowth. Mature mineralized bone was present throughout a significant portion of the implant, especially in the macropores (figure 41). Osteoid, the matrix initially deposited during bone formation, filled the majority of the implant voids, including the microporous structure, by four months. Direct bone bonding was evident in all samples, with no intervening connective tissue layer separating the implant material and host bone. There was no evidence of overlying epithelial down-growth in to any aspect of the implants.

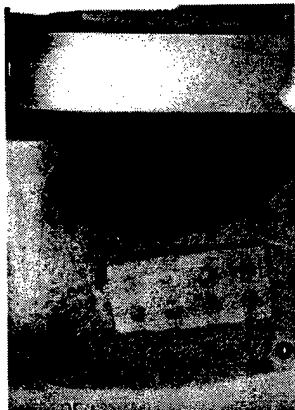


Figure 40. Radiograph of SLS formed implant *in vivo*, at three months. Bone fills the macropores and covers the implant.



Figure 41. An intervening layer of mature bone separates gingival tissue (left) from the implant material (right). A macropore is filled with mature bone. Microporous implant structure shows evidence of bony infiltration.

Two preclinical trials were proposed in the scope of the phase II effort. The first trial, a calvarial defect in a rabbit model, was proposed to study the safety and efficacy of SLS fabricated implants in nonloaded sites. The second trial, a mandibular angle defect in a pig model, was proposed to demonstrate the process and efficacy of SLS fabricated implants derived from anatomical CT data in nonloaded sites. Due to the very encouraging results from the phase I trials, the necessity of the proposed preclinical trials was questioned in favor of more clinically relevant studies that would facilitate subsequent human clinical trials.

BME initiated discussions with clinicians at Wilford Hall Medical Center (WHMC) and the MacKown Dental Laboratory at Lackland Air Force Base (LAFB), San Antonio. These discussions precipitated interest in custom formed synthetic bone from several groups. In particular, Col. Michael Mills and Lt.Col. Vincent Takacs, both of the Department of Periodontics, at MacKown Dental Laboratory, expressed interest in performing a preclinical study with custom formed synthetic bone precursory to further clinical trials in humans. The preclinical trial would involve direct participation of periodontic students for the purpose of fulfilling research and clinical application requirements. A protocol was developed, which is currently undergoing evaluation by the Clinical Investigation Directorate (CID) at LAFB, and is expected to be approved towards the end of the year.

The proposed study will extend results of the canine study discussed above to encompass the complete custom implant methodology. In the previous canine study, SLS fabricated implants of regular geometry were implanted into a surgically created

defect. In the proposed study, the healing response to custom formed synthetic bone implants will again be examined in surgically created alveolar defects. Rather than using regular shaped implants for each defect, implant shape, size, and fit will be derived through three-dimensional reconstruction of CT-image data of the defect sites.

The study is planned to last 24 weeks (figure 41). Defects will be surgically created bilaterally in nine minipigs. (The animal model was changed due to increased sensitivity in the military to the use of canines in medical research). The animals will be allowed to heal twelve weeks prior to CT image data acquisition, fabrication of custom implants, and implant placement. The twelve-week healing period is current practice in this type of reconstruction. The implants will be fabricated as before using SLS and the implants will be designed to incorporate custom features to promote tissue ingrowth guidance. Control side defects will be filled with particulate hydroxyapatite and a Gore-Tex® membrane placed over the defect/implants. This defect treatment modality is well known to the periodontics group at LAFB and, therefore, will provide an excellent reference for performance of the custom fabricated synthetic implants. All implants will be harvested at twelve weeks implantation and analyzed histomorphometrically.

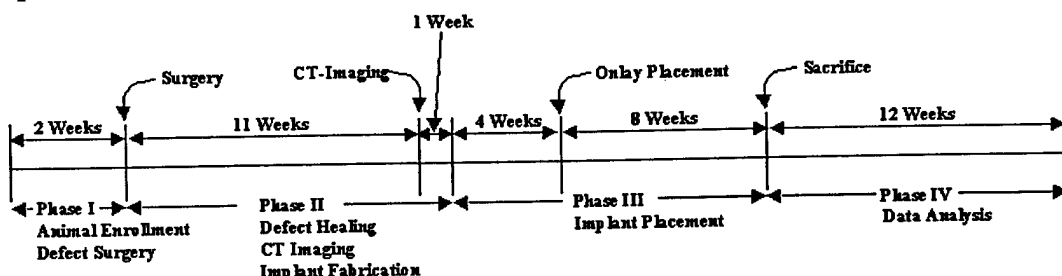


Figure 42. Proposed timeline for alveolar ridge defect study in pigs.

The periodontics group at LAFB has indicated the need to demonstrate the complete custom implant process before proceeding to human clinical studies, which would be the next logical step pending success of the proposed animal study. Other groups at Wilford Hall Medical Center have indicated strong interest in pursuing clinical evaluation of custom formed synthetic implants in humans pending success of the proposed animal trial.

Task Group 5 - Medical Standardization

This group of tasks is completed as processes and methods come online. The major tasks of this group are concerned with qualification of materials, materials inventory control, device packaging, sterilization, labeling and tracking, and overall manufacturing process validation.

BME has identified the raw materials necessary to manufacture custom formed synthetic bone implants. The raw materials and their suppliers are summarized in table 5. Most of the suppliers, with the exception of Rhone-Poulenc, provide certified chemical assays of the respective raw materials. The powder substrate precursor materials supplied by Rhone-Poulenc must be certified for composition on delivery. BME uses inductive coupled plasma (ICP) spectroscopy to determine calcium and phosphorous content and x-ray diffraction (XRD) to determine crystalline phase.

Tracking of these materials is easily integrated into BME's present materials inventory practices. Materials Safety Data Sheets are in place for all materials.

Table 5. Raw materials list and suppliers.

Component	Raw Material	Supplier
Powder Substrate	Dicalcium Phosphate Monocalcium Phosphate	Rhone-Poulenc
Polymer Binder	Methyl Methacrylate n-Butyl Methacrylate Potassium Persulfate Sodium Hydrogen Carbonate Potassium Chloride Sodium Hydroxide	Aldrich Chemical Co.
	Sodium Dodecyl Sulfate	Acros
	iso-Octyl Mercaptopropionate	Phaltz & Bauer
Infiltrating Solutions	Orthophosphoric Acid Methanol	Aldrich Chemical Co.
	Sodium Dodecyl Sulfate	Acros
Chemical Analysis	1N Sodium Hydroxide Phenolphthalein	Aldrich Chemical Co.

Standarization tasks related to implant packaging, including packaging method, implant and package sterilization, and package labeling, were not implemented during the phase II effort due to pending definitions of packaging requirements.

Process validation is pending further quantification of materials formulation and implant manufacturing processes. Most of the methodologies were discussed in **Materials Formulation**. Once all methods are formalized, a series of standard geometrical objects will be fabricated. Their mechanical, physical, and dimensional characteristics will be quantified at each process step and compared to previous results. The goal is to define an operating window for each step in the manufacturing process that will yield an object with an optimal range of properties. Ultimately, the entire implant fabrication process will be treated as a black box that will produce an object with specific properties from an input material with specific properties. The operation of the fabrication process will be governed by quantified constitutive relationships that define the output properties for a given set of input conditions. These constitutive relationships will be used as design criteria at the implant design stage to produce a model description suitable to input to the fabrication process.

Task Group 6 - FDA Milestones

Discussions concerning FDA approval for custom formed synthetic bone implants are in progress. Current indications are it may be most advantageous to pursue 510(k) approval of commodity type implants prior to or parallel to obtaining some form of approval for custom type implants. The 510(k) route would allow approval of a variety of SLS fabricated commodity (i.e. common geometrical shapes) implants with integrated complex features, such as porosity, pore structure, etc., based on similar predicate devices. This will provide the opportunity to prove the viability of the SLS fabricated implants and will provide important data for subsequent approval requirements for patient specific custom anatomical implants.

Conclusions

BME has successfully implemented a pilot facility to fabricate calcium phosphate implants using anatomical data coupled with the selective laser sintering process. Fabrication of commodity and anatomical shapes has been demonstrated. Work is continuing to streamline the pilot facility to efficiently and reproducibly fabricate calcium phosphate implants with desired mechanical, physical, and dimensional properties.

References

1. Capano, P.J., The chemical synthesis, and biomedical and bidental applications of the first truly successful, *in vivo* replacement for bones, teeth, and similar materials, Ph.D. Dissertation, The University of Texas at Austin, 1987.
2. Lagow, R.J., P.J. Capano, S.S. Hoffman, *et al.*, "Calcium bioceramic implants in canine mandibular block defects," *J. Dent. Res.*, **70**, 41A (1991).
3. Nelson, S.R., L.M. Wolford, R.J. Lagow, P.J. Capano, and W.L. Davis, "Evaluation of new high-performance calcium phosphate bioceramics as bone graft materials," *J. Oral Maxillofacial Surg.*, **51**, 1363-1371 (1993).
4. Deckard, C.R., Method and apparatus for producing parts by selective sintering, U.S. Patent 4,863,538, Sept. 5, 1989.
5. Bourell, D.L., J.J. Beaman, H.L. Marcus, and J.W. Barlow, "Solid freeform fabrication: An advanced manufacturing approach," *Solid Freeform Fabrication Symposium Proceedings*, **1**, 1 (1990).
6. Ashley, S., "Rapid prototyping systems," *Mech. Eng.*, **113** [4], 34 (1991).
7. Bourell, D.L., J.J. Beaman, H.L. Marcus, J.W. Barlow, and C.R. Deckard, Multiple material systems for selective beam sintering, U.S. Patent 5,076,869, Dec. 31, 1991.
8. Vail, N.K. and J.W. Barlow, "Microencapsulation of finely divided ceramic powders," *Solid Freeform Fabrication Symposium Proceedings*, **1**, 8 (1990).
9. Bartels, K.A., R.H. Crawford, S. Das, S. Guduri, A.C. Bovik, K.R. Diller, and S.J. Aggarwal, "Fabrication of Macroscopic Solid Models of Three-Dimensional Microscopic Data by Selective Laser Sintering," *Journal of Microscopy*, **169** [3], 383-389 (1993).
10. Levy, R.A., S. Guduri, and R.H. Crawford, "Preliminary Experience with Selective Laser Sintering (SLS) Models of the Human Temporal Bone", *Solid Freeform Fabrication Symposium Proceedings*, **3**, 161 (1992).
11. Barlow, J.W., G. Lee, R.H. Crawford, J.J. Beaman, H.L. Marcus, and R.J. Lagow, Method for fabricating artificial bone implant green parts, U.S. Patent 5,639,402, June 17, 1997.
12. Vail, N.K., J.J. Beaman, H.L. Marcus, D.L. Bourell, and J.W. Barlow, "Development of a poly(methylmethacrylate-*co*-*n*-butylmethacrylate) copolymer binder system," *J. Appl. Polym. Sci.*, **52** [6], 789-812 (1994).
13. Vail, N.K., Preparation and Characterization of Microencapsulated, Finely Divided Ceramic Powders for Selective Laser Sintering, Ph.D. Dissertation, The University of Texas at Austin, 1994.

-
- 14. Vail, N.K., M. Glazer, and J.W. Barlow, "Drying of Colloidal Binder Infiltrated Ceramic Green Parts Produced by Selective Laser Sintering," *Solid Freeform Fabrication Symposium Proceedings*, 4, 333-338 (1993).
 - 15. Wexler, A. and S. Hasegawa, "Relative humidity-temperature relationships of some saturated salt solutions in the temperature range 0° to 50°C," *Journal of Research of the National Bureau of Standards*, 53 [1], 19-25 (1954).
 - 16. Encyclopedia of Polymer Science and Engineering, J. Wiley and Sons, Inc., New York, 1986.
 - 17. Faust, G.T., W.L. Hill, and D.S. Reynolds, "The binary system P₂O₅-2CaO•P₂O₅," *Am. J. of Sci.*, 242, 447-477 (1944).
 - 18. Frenkel, J., "Viscous flow of crystalline bodies under the action of surface tension," *J. Phys. (USSR)*, 9 [5], 385 (1945).